1-1-2023

Heterogeneous microstructure and mechanical behaviour of Al-8.3Fe-1.3V-1.8Si alloy produced by laser powder bed fusion

S. J. Yu

P. Wang

H. C. Li

R. Setchi

M. W. Wu

See next page for additional authors

10.1080/17452759.2022.2155197

Yu, S. J., Wang, P., Li, H. C., Setchi, R., Wu, M. W., Liu, Z. Y., ... & Zhang, L. C. (2023). Heterogeneous microstructure and mechanical behaviour of Al-8.3 Fe-1.3 V-1.8 Si alloy produced by laser powder bed fusion. Virtual and Physical Prototyping, 18(1), Article e2155197. https://doi.org/10.1080/17452759.2022.2155197

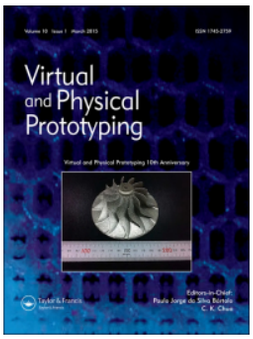

Virtual and Physical Prototyping

ISSN: (Print) (Online) Journal homepage: https://www.tandfonline.com/loi/nvpp20

Heterogeneous microstructure and mechanical behaviour of Al-8.3Fe-1.3V-1.8Si alloy produced by laser powder bed fusion

S.J. Yu, P. Wang, H.C. Li, R. Setchi, M.W. Wu, Z.Y. Liu, Z.W. Chen, S. Waqar & L.C. Zhang

To cite this article: S.J. Yu, P. Wang, H.C. Li, R. Setchi, M.W. Wu, Z.Y. Liu, Z.W. Chen, S. Waqar & L.C. Zhang (2023) Heterogeneous microstructure and mechanical behaviour of Al-8.3Fe-1.3V-1.8Si alloy produced by laser powder bed fusion, Virtual and Physical Prototyping, 18:1, e2155197, DOI: 10.1080/17452759.2022.2155197

To link to this article: https://doi.org/10.1080/17452759.2022.2155197

Published online: 23 Dec 2022.

VIRTUAL AND PHYSICAL PROTOTYPING
2023, VOL. 18, NO. 1, e2155197 (18 pages)
https://doi.org/10.1080/17452759.2022.2155197

Taylor & Francis
Taylor & Francis Group

Heterogeneous microstructure and mechanical behaviour of Al-8.3Fe-1.3V-1.8Si alloy produced by laser powder bed fusion

S.J. Yu[a,b], P. Wang [a,b], H.C. Li[c], R. Setchi [d], M.W. Wu[e], Z.Y. Liu[a,b], Z.W. Chen[a,b], S. Waqar[f] and L.C. Zhang[g]

[a]Additive Manufacturing Institute, Shenzhen University, Shenzhen, People's Republic of China; [b]Guangdong Key Laboratory of Electromagnetic Control and Intelligent Robotics, College of Mechatronics and Control Engineering, Shenzhen University, Shenzhen, People's Republic of China; [c]School of Materials Science and Engineering, Shanghai University of Engineering Science, Shanghai, People's Republic of China; [d]Cardiff School of Engineering, Cardiff University, Cardiff, UK; [e]Department of Materials and Mineral Resources Engineering, National Taipei University of Technology, Taipei, Taiwan; [f]Department of Mechanical Engineering, Institute of Space Technology, Islamabad, Pakistan; [g]School of Engineering, Edith Cowan University, Perth, Australia

ABSTRACT

The relationship between processing parameters, microstructure, and mechanical properties of Al-8.3Fe-1.3V-1.8Si alloy processed by laser powder bed fusion is seldom studied. Therefore, fully dense alloys with two parameters were selected to investigate this key issue. The results show that the alloy with low power and scanning speed (S200) shows fan-shell-shaped melt pools and laser tracks while another (S350) shows a deeper and wider melt pool. Both alloys obtain a heterogeneous microstructure without a secondary phase in melt pool (MP) and a nano-sized phase in melt pool boundary (MPB). The difference between solid-solution strengthening and Orowan strengthening in MP and MPB contributes to the difference in compressive yield strength (S200: 380 ± 14 MPa and S350: 705 ± 16 MPa), and heterogeneous nano-hardness results in different crack behaviours and failure strains. This work indicates that adjusting processing parameters is an effective method to control microstructure and mechanical properties of this alloy.

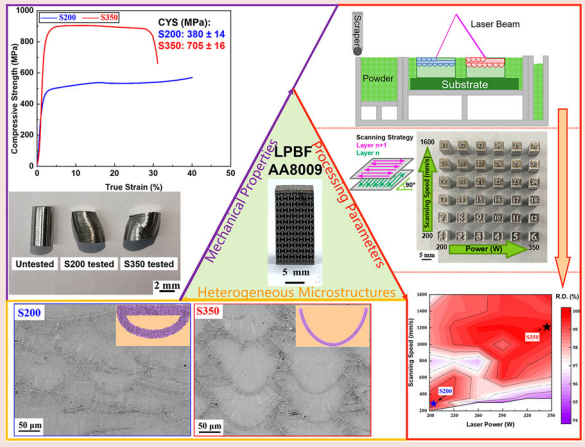

ARTICLE HISTORY
Received 12 September 2022
Accepted 30 November 2022

KEYWORDS
Laser powder bed fusion; Al-Fe-V-Si alloy; heterogeneous microstructure; mechanical properties

1. Introduction

Laser powder bed fusion (LPBF, also called Selective Laser Melting) is one of the most widespread additive manufacturing technologies that can produce metallic components by computer-aided designs (CADs) (Attar et al. 2015; Chen et al. 2021). LPBF technology offers many advantages compared with conventional processes in terms of design flexibility, cost savings, energy savings, the flexibility of processing parameters, and adaptable cooling rates that can reach up to 4×10^7 K/s (Didier et al. 2021; Hooper 2018; Zhao et al. 2022). With long-term research, Al-based alloys such as Al-Cu (Wang et al. 2018), Al–Si (Wang et al. 2021), Al-Mg (Wang et al. 2019) and Al-Zn (Wang et al. 2017)

CONTACT P. Wang peiwang@szu.edu.cn Additive Manufacturing Institute, Shenzhen University, Shenzhen, People's Republic of China; Guangdong Key Laboratory of Electromagnetic Control and Intelligent Robotics, College of Mechatronics and Control Engineering, Shenzhen University, Shenzhen, People's Republic of China

This article has been corrected with minor changes. These changes do not impact the academic content of the article.

have been successfully fabricated and several key obstacles during LPBF processing have been overcome. Moreover, LPBF has also triggered the development of novel alloys that are specific to the LPBF process for the fabrication of components with improved performance and functionalities. For example, elevated-temperature Al alloys like Al-Ni (Deng et al. 2022) or Al-Sc (Koutny et al. 2018) alloys have been successfully fabricated by LPBF, thereby causing the design and fabrication of LPBFed high-temperature Al alloys to be a heated topic with a focus on aeronautical, astronautical, and automotive components such as impellers, valves, pistons and missile vines (Michi et al. 2022). In addition, the researches about tailoring microstructure by processing parameters to meet the demand of the LPBFed components with complex structures designed for exhibiting balanced attributes (ultralight weight, ultrahigh bearing capability, extreme heat resistance and high reliability) have been hot topic in the field of LPBFed Al alloys (Zhao et al. 2022; Wu et al. 2021).

AA8009 Aluminum alloy, developed by Skinner et al. in 1986 (Skinner et al. 1986), is regarded as an aluminum alloy applied at a temperature of around 673 K (Zheng et al. 2015). Owing to its attractive properties at mid-temperature (Goyal et al. 2019; Deng et al. 2020), such as high specific strength, ductility, and fracture toughness (Skinner et al. 1986; Franck and Hawk 1989), AA8009 alloy has considerable applications in the aerospace and automobile industries to replace Ti alloys (Wang et al. 2007; Li et al. 2003). Therefore, in recent decades, AA8009 alloy has been widely processed in many different ways, such as mixed solid–liquid casting (Sahoo, Sivaramakrishnan, and Chakrabarti 2000), planar flow casting (Yaneva et al. 2004), spray deposition (Yan et al. 2007), linear friction welding (Koo and Baeslack 1992), and friction stir processing (Nouri, Taghiabadi, and Moazami-Goudarzi 2020) for manufacturing aircraft and aerospace heat resistant components (Gilman et al. 1988). However, due to the relatively low cooling rate involved with these processes, they cannot fulfil the demand of forming the $Al_{12}(Fe, V)_3Si$ phase that can be stable as sphere-shaped dispersoids and quasistatic body-centered cubic (BCC) structure up to 773 K (Carreño et al. 1998). Thus, LPBF technology with a high cooling rate has the potential for fabricating AA8009 components with exceptional properties, which can result in a non-equilibrium microstructure and therefore a remarkable performance (Wang et al. 2021) while the gradient distribution of the cooling rate around the melt pool generates different phases which leads to different mechanical properties and microstructures around the melt pool.

Early studies suggested that AA8009 alloy fabricated by LPBF (Sun et al. 2015b) and electric beam melting (EBM) (Sun et al. 2016) can obtain a higher hardness of 246 HV (Sun et al. 2016) and 153 HV (Sun et al. 2015a), respectively, which are higher than that of AA8009 alloy fabricated by conventional casting (45 HV) (Zheng et al. 2015). However, Sun et al. (Sun et al. 2017) found that the LPBF processed samples encountered regular cracks on the surfaces which could lower the hardness, mechanical properties, and ductility. It was demonstrated that aluminum alloy exhibited a strong sensitivity for crack formation due to its large solidification temperature range, high thermal expansion, and large solidification shrinkage. Sun et al. (Sun et al. 2017) also showed that by increasing the scanning speed and hatch distance, the laser pre-heating procedure could suppress the formation of cracks. However, no comprehensive work was currently done on the relationship of the parameters, microstructures, and mechanical properties of LPBFed AA8009 alloy, which is essential to control the microstructures and mechanical properties by adopting different parameters for designing and fabricating the components with the multi-performance to meet the demand of complex application environments (Wang et al. 2022).

In this work, the densification behaviour of LPBF fabricated AA8009 alloy was investigated by altering different processing parameters. The near-fully dense LPBFed AA8009 alloy samples fabricated by two different optimised parameters were selected and examined to clarify the relationship between processing parameters and microstructures as well as the mechanical properties of LPBFed AA8009 alloy. The findings in the current work are expected to provide a new pathway for developing high-strength and fine-microstructure AA8009 alloy by LPBF.

2. Experimental details

2.1. Materials & LPBF processing

Al-8.3Fe-1.3V-1.8Si alloy (AA8009) powders were prepared by gas atomisation (nominal composition: 8.28 wt% Fe, 1.34 wt% V, 1.81 wt% Si, and balanced Al). The powder particle with a size ranging between 15 and 53 μm (D_{50} = 30.5 μm) (Figure 1(a)), was supplied by Changsha Advanced Materials Industrial Research Institute Co., Ltd. The spherical morphology of the raw AA8009 alloy powder and its corresponding microstructure is shown in Figure 1(b). Small satellites were noted around the spherical AA8009 powders and a coarse dendrite phase composed of Al, Fe, V, and Si atoms was dispersed in the Al matrix.

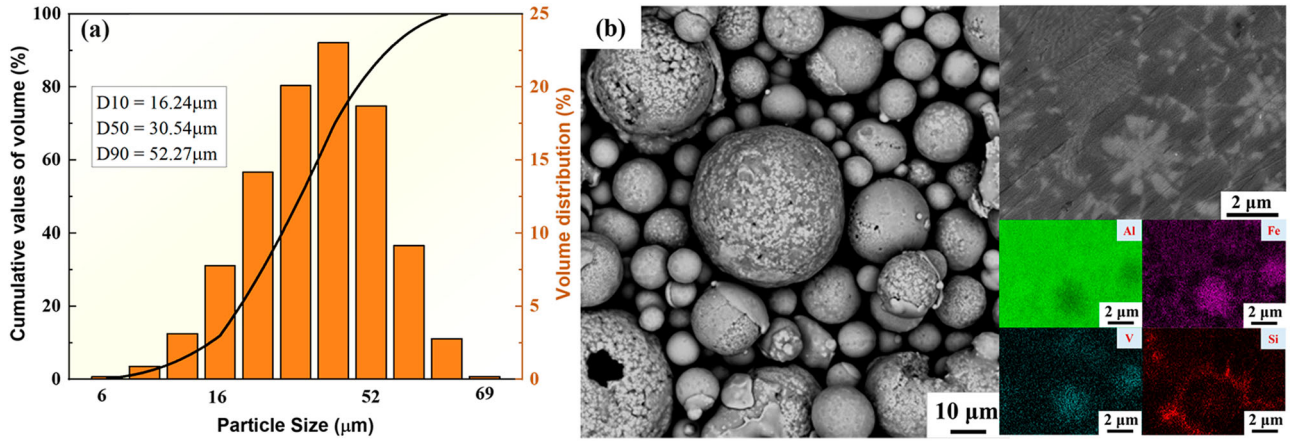

Figure 1. (a) Powder particle size distribution with normal distribution fit of AA8009 alloy (b) SEM micrographs for AA 8009 alloy powder and corresponding EDS maps for AA 8009 alloy powder.

Cuboid specimens (5 mm × 5 mm × 10 mm) for density and microstructure characterisation, and cylindrical rods (Ø 3 mm × 6 mm) for mechanical tests and fracture observation were fabricated under a protective argon atmosphere (> 99.999 wt% purity) using a DiMetal-100 system (Laseradd Additive Technology Co., Ltd.) equipped with a 500 W Nd: YAG laser (continuous wave).

Volumatic energy density (E_v) has an impact on the quality of the samples (Gustmann et al. 2016), which is given by (Gu, Chang, and Dai 2014):

$$E_v = \frac{P}{v_s \cdot l_{hs} \cdot l_z} \tag{1}$$

where P is the laser power input (W), v_s is the laser scanning speed (mm/s), l_{hs} is the hatch spacing (mm) and l_z is the layer thickness (mm). According to the current work (Yu et al. 2022; Yang et al. 2022; Cacace and Semeraro 2021; Sing et al. 2021), the parameters were controlled for the optimisation as follows: the laser power was varied between 200 and 350 W (i.e. 200 W 230 W 260 W 290W 320W and 350W), and the laser scanning speed was selected between 200 and 1600 mm/s (i.e. 200 mm/s 250 mm/s 300 mm/s 350 mm/s 400 mm/s 600 mm/s 800 mm/s 1000 mm/s 1200 mm/s 1400 and 1600 mm/s). Due to the powder size distribution (15 ~ 53 μm), layer thickness (l_z) was selected as 0.05 mm, respectively. The hatch spacing (l_{hs}) and hatch style rotation were selected as 0.08 mm and 90°, respectively, which is based on the current results (Sun et al. 2022; Sing 2022; Bouabbou and Vaudreuil 2022; Koh et al. 2022) and the need for the analysis. All samples were fabricated under a single melt continuous scanning strategy (Prashanth, Scudino, and Eckert 2017).

2.2. Characterisation

The density of the samples was determined using the Archimedes method (standard GB/T3299-1996). Phase analysis was performed by X-ray diffraction (XRD, Cu-Kα, Rigaku MiniFlex 600 PRO) in a Bragg–Brentano configuration and electron probe micro analyzer (EPMA, SHIMADZU, EPMA-8050G). An optical microscope (OM, Keyence VHX-500) was used for observing the defects in the morphologies of the sample during parameter optimisation. A field emission scanning electron microscope (FE-SEM, FEI-Quanta 450-FEG, United States) was used for microstructure characterisation. FE-SEM device was equipped with an energy-dispersive X-ray spectroscopy detector (EDS) and an electron backscatter diffraction device (EBSD, EDAX-TSL system). For characterisation, the samples were cut along the building direction, ground with sandpaper (P240-P4000), and polished with MasterMet 2 (Buehler GmbH) using a vibromet facility. All samples were cut along the building direction for characterisation.

Thin foil specimens were extracted from two specific areas (the centre of the melt pool and the area that crossed the bottom of the melt pool boundary) using a focused ion beam (FIB, FEI, Scios) device with ultra-high-resolution SEM capability at an accelerating voltage of 30 kV. A Pt protective layer was deposited on the surface of the specimens and the final milling process was conducted at an accelerating voltage of 2 kV to avoid possible damages or thermal recrystallization. A transmission electron microscope (TEM, Talos F200S G2) equipped with an X-ray energy dispersive spectrometer (EDS, EDAX Apollo X) operated at 300 kV was used to reveal the local microstructure and nano-precipitates.

2.3. Mechanical properties

Vickers microhardness tests were carried out along the building direction using a Future-Tech FM-110 microhardness tester with a 0.1 kg load and 10 s dwell time. Multiple measurements were taken at random locations for each sample. The mean value of around 20 random measurements was considered as the representative hardness for each specific case. Room-temperature compression tests were performed with the loading axis parallel to the building direction using a universal material machine (E44.304, MTS Co, the United States) at a constant crosshead speed of 0.001 mm/s according to the DIN 50106 standard (Attar et al. 2014). Five specimens were measured to ensure the reproducibility of the results. The nano-indenter (Hysitron Ti-950) was used to investigate the nano-hardness across the melt pool. Fourteen triangular loading-unloading patterns with the indentation spacing of 6 μm were applied under the same condition (a maximum load of 5 mN, a loading-unloading period of 5 s, and a holding period of 5 s).

2.4. Governing equations and numerical modelling description

2.4.1. Thermal governing equations and heat source model

The 3D heat transfer governing equation is given by Fourier's heat transfer equation:

$$\frac{\partial}{\partial x}\left(k_x(T)\frac{\partial T}{\partial x}\right)+\frac{\partial}{\partial y}\left(k_y(T)\frac{\partial T}{\partial y}\right)+\frac{\partial}{\partial z}\left(k_z(T)\frac{\partial T}{\partial z}\right)+Q = \rho(T)C(T)\frac{\partial T}{\partial t} \quad (2)$$

Where k_x, k_y and k_z are the thermal conductivities in x, y and z directions, Q is the heat generation per unit volume, p is the material density, C is specific heat capacity, T is temperature, and t is time. Since anisotropic thermal conductivity was assumed, therefore Eq. (2) can be simplified as:

$$k(T)\frac{\partial^2 T}{\partial x^2}+k(T)\frac{\partial^2 T}{\partial y^2}+k(T)\frac{\partial^2 T}{\partial z^2}+Q = \rho(T)C(T)\frac{\partial T}{\partial t} \quad (3)$$

Where $k(T)$ is the isotropic thermal conductivity of the material. Since all three heat transfer modes including conduction, convection and radiation were considered. Therefore, the classical thermal equilibrium equation was given:

$$k\left(\frac{\partial T}{\partial n}\right)+h(T-T_0)+\varepsilon\sigma(T^4-T_0^4)-q = 0 \quad (4)$$

Where k is thermal conductivity, h is convection coefficient, ε is radiation emissivity, σ is Stephen Boltzmann constant, and q is input heat flux.

As the continuum approach was adopted, and different regions were assigned with different phases initially, therefore density in the powder and solid phases were considered to be not uniform and depend on the percentage porosity of the powder bed. The porosity-dependent density can be given by (Waqar et al. 2020):

$$\rho_p = (1-\varphi)\rho_s \quad (5)$$

Where ρ_p is powder phase density, ρ_s is solid phase density, and φ is the percent porosity of the powder bed. Similarly, thermal conductivity was also considered to be phase-dependent therefore, thermal conductivity in powder and solid phases are related by (Waqar, Guo, and Sun 2021, 2022):

$$k_p = (1-\varphi)^4 k_s \quad (6)$$

Where k_p is the thermal conductivity of the powder phase, k_s is the thermal conductivity of the solid phase, and φ is the percentage porosity of the powder bed.

The commonly adopted gaussian heat source model was used. A complete 3D volumetric gaussian heat source with exponential decay along the layer thickness was used and can be given by:

$$Q = \frac{2\eta P}{\pi R^2 S}\exp\left(-\frac{2((x-vt)^2+y^2)}{R^2}\right)\exp\left(\frac{-|z|}{S}\right) \quad (7)$$

Where η is the laser absorptivity of material, P is laser power, S is the laser penetration depth in the material which was considered equal to a unit layer thickness, and R is the laser beam radius corresponding to the point where laser irradiance diminishes to $1/e^2$.

2.4.2. Numerical model description and meshing sequence

To understand the process dynamics and melt pool generation and dimensions, the process was also computationally simulated. The thermal simulations were performed on the commercial software package ABAQUS. A uni-layer uni-track model was created to simulate the process with minimum computational cost. The model consists of a baseplate region with dimensions of 2 mm × 2 mm and a thickness of 0.5 mm. The powder bed region consists of 1.2 mm × 1.2 mm and a thickness equal to the experimental layer thickness (i.e. 50 μm). The powder bed region was fine meshed with heat transfer brick element DC3D8. The mesh size in the powder region was 40 μm × 40 μm × 25 μm, based on the established meshing sequences in previous research works. The

baseplate region was finely meshed close to the powder bed region and coarse meshed away from the base plate to reduce the computational cost. User-defined subroutines USDFLD and DFLUX were used to simulate the phase change from powder to the liquid and subsequently solid phase and moving heat source modelling respectively.

To accurately simulate the large baseplate, ambient boundary condition was applied to the lower surface of baseplate. All three modes of heat transfer (i.e. conduction, convection, and radiation) were considered. Both the convection and radiation were applied as boundary conditions on the top surface, since only the top surface is exposed to the surroundings. All the adopted numerical values for different constants are also presented in Table 1.

The melt pool size was measured by adjusting the scale and applying a limit of melting temperature of Al-8.3Fe-1.3V-1.8Si alloy (i.e. 933 K) (Srivastava, Ojha, and Ranganathan 1998). The region with a temperature beyond the defined limit was considered as the melt pool size. The simulated melt pool sizes were then compared with experimental results for validation purposes.

3. Results and discussion

3.1. Parameter optimisation and densification

Figure 2(a) shows the relationship between the RD, the scanning speed (V), and the laser power (P) of the processed samples. Figure 2(b, c) shows a fine surface morphology of the S200 and the S350 samples with few defects observed. Figure 2(d) presents the morphology of the sample processed with the laser power of 200 W and the scanning speed of 800 mm/s, which has a volumetric energy density of 62.50 J/mm^3 according to Eq. (1). Transgranular cracks are observed along the melt pool boundary during the processing due to the relatively high cooling rates during the LPBF processing (10^3-10^7 K/s). Similarly, Kou (Kou 2015) considered the grain boundary critical to crack formation, especially in rapidly cooled Al–Fe alloys which are susceptible to cracks (Pauly et al. 2013; Sun et al. 2017).

Table 1. LPBF processing parameters used in simulation (Sun et al. 2015; Srivastava, Ojha, and Ranganathan 1998; Lienert, Nagy, and Baeslack 1998).

Processing parameter	Value
Melting Point	933 K
Laser absorptivity, A	0.09
Percentage porosity of powder layer, φ	50%
Optical penetration depth, S	0.05 mm
Thermal Conductivity, k	95 W/m·k
Thermal convection coefficient, h	10 W/m^2·k
Emissivity, ε	0.2

As shown in Figure 2(e), the sample with the laser power of 350 W and the scanning speed of 400 mm/s (volumetric energy density of 250 J/mm^3) displays the large spherical pores caused by the high volumetric energy density (Sun et al. 2017; Wang et al. 2018), which are different from the small keyhole formed at the melt pool boundary. Therefore, according to the above discussion, a relatively higher E_v (70 - 180 J/mm^3) can lead to a higher temperature of the melt pool during processing, which would further decrease the formation of cracks. Meanwhile, with increasing E_v, more pores were formed, which would deteriorate the RD (Wang et al. 2018; Zhang et al. 2011). Therefore, achieving fully dense alloys fabricated by LPBF cannot rely on predictions exclusively based on the energy density, as reported by several other research (Attar et al. 2014; Pauly et al. 2013).

As shown in Figure 2, it is important to mention that there are two processing windows beneficial for obtaining near-fully dense AA8009 specimens (RD $\geq$ 99%), which are marked by blue star and black star. The sample fabricated with the processing parameter of 200W laser power and 300 mm/s scanning speed (marked by the blue star in Figure 2(a)) has a relative density of 99.72%, which was labelled as S200 (volumetric energy density of 166.67 J/mm^3). Whereas the sample marked by black star fabricated with the laser power of 350W and the scanning speed of 1200 mm/s has a relative density of 99.65%, which was termed as S350 (volumetric energy density of 72.92 J/mm^3). Therefore, these two near-fully dense AA8009 specimens with different parameters were selected to further investigate their microstructure and mechanical properties.

3.2. Microstructure

Figure 3 shows the typical XRD patterns of LPBFed AA8009 samples with two different parameters. The diffraction peaks of a-Al phase (Ravi 2004) and undefined Al–Fe-V-Si phase (Zheng et al. 2015) are identified in the XRD patterns of two LPBFed samples (Figure 3(a)), which shows a similar result compared to the previous research about the rapid solidification Al–Fe-V-Si alloys (Zheng et al. 2015; Sun et al. 2015a; Tang et al. 2007). As shown in Figure 3(b), the (111) peak of the α-Al phase of the S350 sample shifts from 38.60° to that of the S200 sample (38.23°), suggesting that the increase in solute concentration in Al-based solid solutions due to large solute atoms (Fe, V, Si) compared to the solvent Al atoms. According to the crystallography, the lower interplanar spacing of Al in the S350 sample leads to a lower lattice constant calculated by XRD results (0.404 nm) compared to the S200 sample (0.407 nm) (Huang,

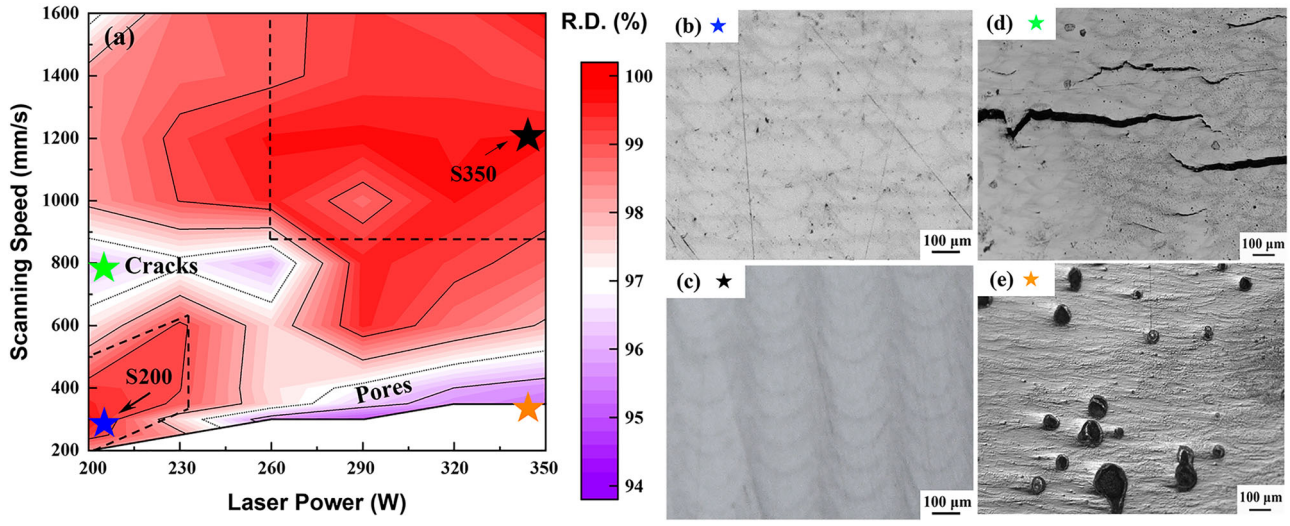

Figure 2. (a) Contour map of the relative density (RD) of the LPBFed AA8009 samples as a function of scanning speed and laser power. (b-e) The morphologies of the sample were fabricated with (b) S200 parameter (c) S350 Parameter (d) 200 W laser power and 800 mm/s scanning speed of the green star, (e) 350 W laser power and 400 mm/s scanning speed of the orange star.

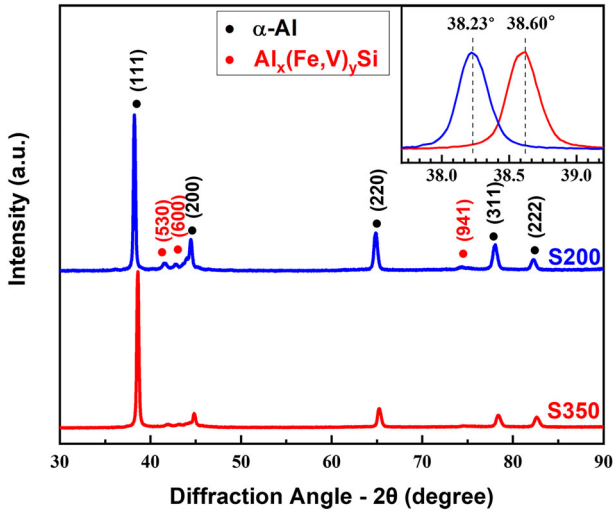

Figure 3. XRD patterns and its close-up view (inset) of LPBF processed AA8009 samples with two different parameters.

Ishihara, and Shingu 1997). The decreasing lattice constant of the S350 sample may result from the higher solid solution of Fe, V, and Si atoms in the Al matrix of the S350 sample. This phenomenon could be supported by the lower intensity of the $Al_x(Fe, V)_ySi$ phase in the S350 sample than that in the S200 sample (Uesugi and Higashi 2013; Prasetya, Muhammad Rifai, and Miyamoto 2020).

Figure 4 depicts the morphologies of two samples viewed along the cross-section of the sample. As shown in Figure 4(a), the microstructure of S200 displays typical fan-shell laser melt pools and the laser melting track, while in Figure 4(b), the morphology of S350 shows a wider and deeper fan-shell shape which is also observed in Al-Sc and Al-Zr alloys (Michi et al. 2022). In order to further study the formation of these typical morphologies, a finite element analysis was carried out by using the ANSYS code, which indicates that the higher laser power can result in a deeper and wider melt pool. According to the finite element analysis, the melt pool area of the S200 sample is 134 μm width × 56 μm depth and the S350 sample have a 155 μm × 74 μm melt pool area, which is consistent with the experimental results shown in Figure 4(a, b).

As shown in Figure 4(a) and (b), the melt pool (MP) area and the melt pool boundary (MPB) area of the processing parameters display an obvious difference in microstructure, which leads to the different morphologies of these two samples. Figure 4(a) shows that the S200 sample has several horizontal melt tracks due to a shallower melt pool caused by the lower power; by contrast, in the S350 sample, the fan-shell-shaped melt pool covers most of the horizontal melt track and the previous layer of melt pool due to the deeper melt pool formed by high laser power. According to EPMA analysis, nano-precipitates containing Fe and V elements are formed in the MPB area. Such a phenomenon in the S350 sample is more significant than in the S200 sample. Meanwhile, the dissolution of Fe, V, and Si at the bottom area of the melt pool boundary is lower compared to the centre due to the higher cooling rate in the centre, resulting in coarser precipitates formed at the bottom of the melt pool. This scenario was also reported in Ref. (Tan et al. 2020). To further analyse the microstructure in the MP area and the MPB area of both samples,

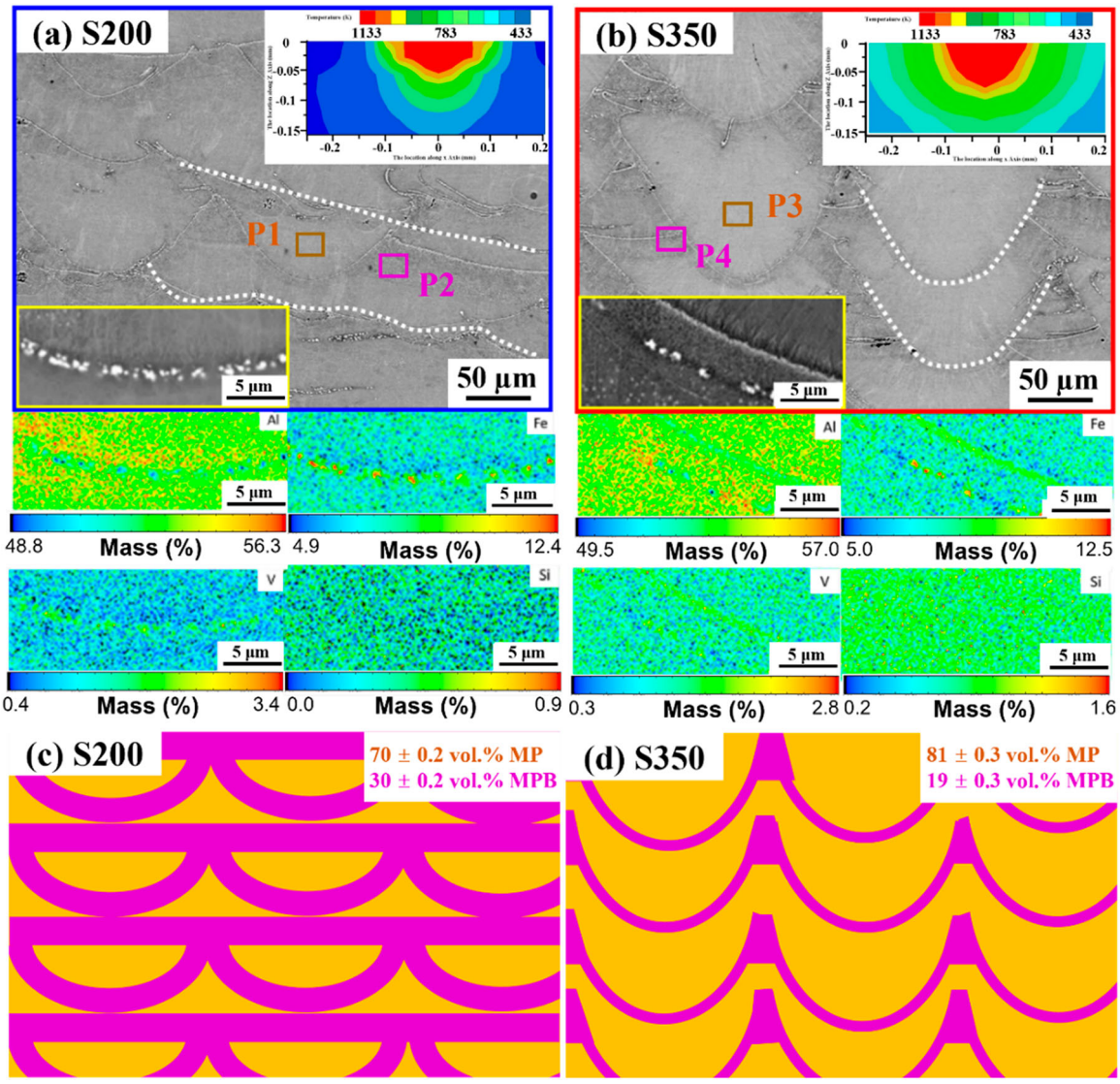

Figure 4. SEM micrographs and EPMA elemental mapping results of LPBFed AA8009 alloy: (a) S200 and (b) S350 samples. Insets are the corresponding finite element analysis graphs showing the thermal distribution during LPBF processing of S200 and S350 samples. Schematic melt pools for (c) S200 and (d) S350 samples based on the experimental microstructures.

thin foil specimens were respectively extracted from the MP area and the MPB area marked as Position 1 (P1), Position 3 (P3), Position 2 (P2), and Position 4 (P4) in Figure 4 (a, b), which would be further characterised by TEM.

To clarify the volume fraction of MP structure and MPB structure in both samples, the volume fraction of each structure has been calculated by Image-Pro Plus software (Version 6.0 Software, Media Cybernetics, Inc. USA); the S200 sample contains 70 ± 0.2 vol. % MP area and 30 ± 0.2 vol. % MPB area and S350 sample includes 81 ± 0.3 vol. % of MP area and 19 ± 0.3 vol. % MPB area. The corresponding volume fraction is depicted in the schematic below (Figure 4(c, d)) to analyse the mechanical mechanism comprehensively.

In order to further analyse the grain morphologies, inverse pole figure (IPF) with grain boundary map of the α-Al phase and geometrically necessary dislocations (GND) for all materials are shown in Figure 5. As displayed in Figure 5(a, b), the columnar grains of both samples are parallel to the building direction caused by the epitaxial growth of Al crystals and the 90°-rotating scanning strategy of processing, which was also observed in LPBFed 316L alloy (Yang et al. 2019) and LPBFed CoCrMo alloy (Zhou et al. 2015). The IPF images demonstrate that both samples predominantly own <111 > fiber texture due to the better stability compared to <100 > fiber texture (Bois-Brochu et al. 2014), which is consistent with the phenomenon in LPBFed Al–Li and Al-Cu alloys which has a < 111 > fiber texture. The EBSD analysis about <111 > fiber texture in LPBFed AA8009 alloys also matches the XRD results. Compared to the S350 sample, more fine grains are observed in

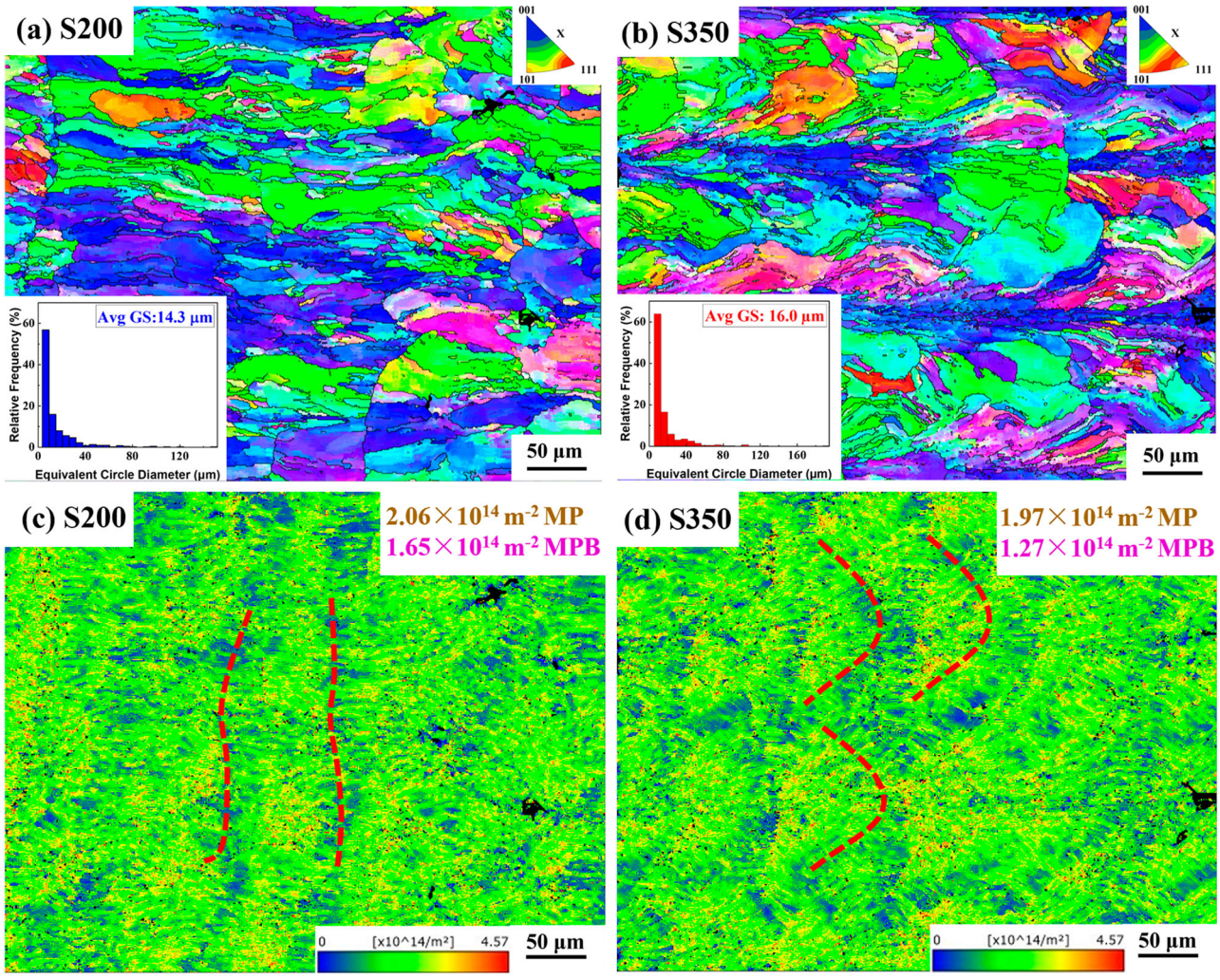

Figure 5. (a, b) Inverse pole figure with grain boundary map (inset: corresponding equivalent grain size diameter in IPF maps) and (c, d) GND density map of LPBF produced AA8009 samples with two different parameters.

S200 (Figure 5(a, b)), which may result from the effect of the low laser power on the grain-growth inhibition as described in Ref. (Liu et al. 2018). Therefore, the S200 possesses a smaller average columnar grain of 14.3 μm while the average columnar grain is higher (16.0 μm) as shown in the dominant microstructural morphology.

As shown in GND distribution maps (Figure 5(c, d)), the LPBFed AA8009 alloys in the MP area and the MPB area have different GND values, which is influenced by the different cooling rate and thermal accumulation (Figure 4(a, b)). Although the sample with low power and high scanning speed (the low volumetric energy density) can obtain the microstructure of the high cooling rate (Saboori et al. 2020), the higher laser power (350W) can cause more significant thermal accumulation to coarsen the precipitates and reduce the residual stress and dislocation density (Wang et al. 2020; Pauly et al. 2018). Therefore, the S350 sample has fewer dislocations (1.97×10^{14} m^{-2} at MP and 1.27×10^{14} m^{-2} at MPB) than the S200 sample (2.06×10^{14} m^{-2} at MP and 1.65×10^{14} m^{-2} at MPB).

Figure 6 shows the high-angle annular dark field scanning transmission electron microscopy (HAADF-STEM) graph and corresponding energy dispersive spectroscopy (EDS) maps of FIB-prepared specimens in the MP area of both samples. The corresponding high-resolution TEM images in Figure 6 show that there are no obvious precipitates generated in α-Al matrix. It indicates that the Fe, V, and Si atoms in both samples have been fully dissolved into α-Al matrix of the MP area with the assistance of a relatively high cooling rate. According to the EDS analysis, the Al matrix contains 11.44 wt% Fe, 1.38 wt% V, and 1.44 wt% Si in the S200 sample, and 12.81 wt% Fe, 1.36 wt% V, and 1.41 wt% Si in the S350 sample. Due to lower volumetric energy density and higher scanning speed during the processing of S350 than that of S200, the cooling rate during the processing of S350 should be higher than

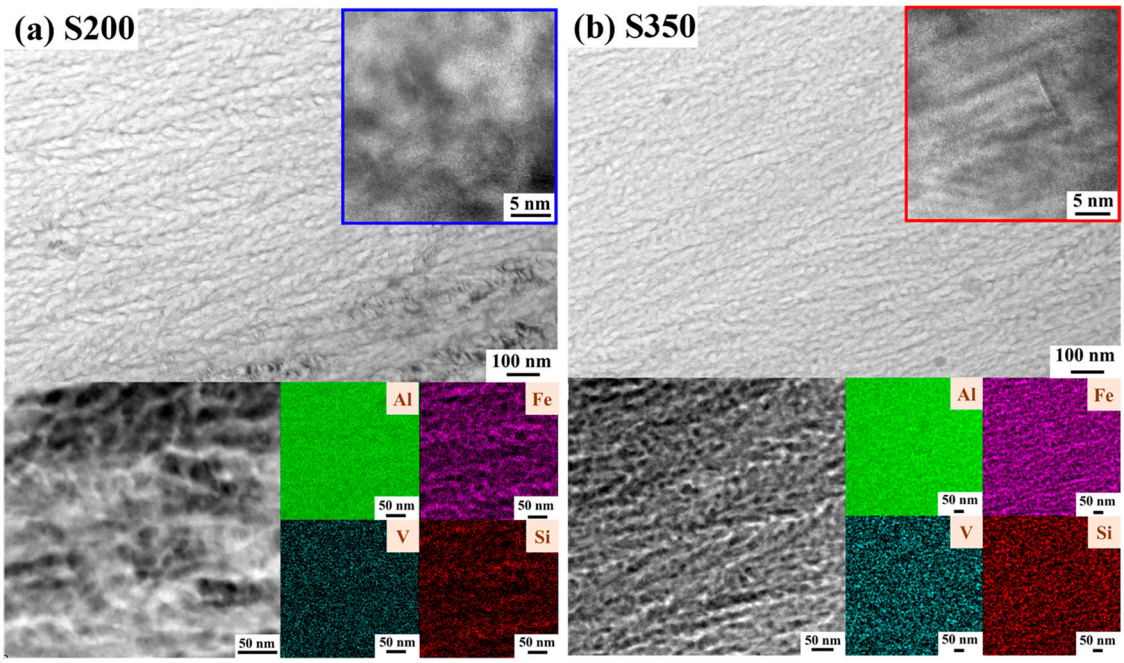

Figure 6. TEM images and corresponding EDS maps at the melt pool area in Figure 4: (a) P1, and (b) P3 (insets: high-resolution graph of each sample in the melt pool area).

that of S200, which phenomena have been confirmed by our previous work (Pauly et al. 2018). Therefore, the S350 sample shows a significantly increased solid solution of Fe atom in the S350 sample compared to that of the S200 sample.

Figure 7 displays the HAADF-STEM graph, its corresponding selected area electron diffraction (SAED) patterns, and EDS maps of FIB-prepared specimens in MPB area of S350 and S200 samples (Figure 4). Figure 7(a) shows that a cellular structure composed of nano-precipitates generates in the upper side of the MPB area and the cell size of precipitates (~ 100 nm) are dispersed uniformly in the MPB area. According to EDS maps, there are few V atoms (1.16 wt%) in the nano-precipitates of cellular structure, which contains 19.02 wt% Fe, 6.46 wt% Si, and 73.36 wt% Al. The precipitates in the MPB area of S200 samples have 22.07 wt% Fe, 3.23 wt% V, 4.19 wt% Si, and 70.59 wt% Al. Based on the analysis of the chemical composition of precipitates, the volume fraction of the precipitates in the MPB zone is 38% and the content of Fe, V, and Si atoms supersaturated in the Al matrix is 0.21 wt% Fe, 0.19 wt% V, and 0.15 wt% Si according to the corresponding EDS maps. By contrast, the S350 sample displays a dendritic morphology in the upper side of the MPB area. The change in morphology can originate from the difference in cooling rate (Sunagawa 1999; Xian et al. 2017; Xian et al. 2017). Similar to the S200, there are also fewer V atoms (1.07 wt%) in the dendritic structure at the upper side of the MPB area and a smaller precipitate with a volume fraction of 40% and the element proportion of (16.08 wt% Fe, 4.99 wt% V, 3.57 wt% Si, and 75.36 wt% Al) are in the MPB area. The element proportion of Fe, V and Si that are supersaturated in the S350 Al matrix are also higher than the S200 sample, with 0.61 wt% Fe, 0.94 wt% V, and 0.40 wt% Si. The higher content of supersaturated atoms is consistent with the analysis of XRD patterns (Figure 3). In addition, it was observed that new tetragonal-shaped precipitates are formed at the MPB area of the S350 sample, and the ratio between Fe and Si atoms in nano-precipitate are 3:1 (5.42% Si and 16.50% Fe). Such a heterogeneous microstructure was reported in AlSi10Mg alloy prepared by LPBF (Liu et al. 2018).

Based on the SAED pattern (Figure 7(a, b)), the lattice constant of the Al matrix for S200 was calculated to be 0.406 and 0.402 nm for S350. It is well-known that the lattice of the Al matrix reduces finitely with the increasing content of the solute atoms in Al (Uesugi and Higashi 2013). Therefore, the larger lattice constant of the Al matrix indicates that there is a low solid solubility of solute atoms in the Al matrix of S200, which is consistent with the result of the XRD graph (Figure 3). The S350 sample has a higher proportion of Fe and V in fine precipitates dispersed in MPB area than S200 sample, which has a BCC structure identified by SAED pattern. Based on this analysis, the precipitates may be $Al_{12}(Fe, V)_3Si$ phase, which is usually formed at a high cooling rate (Tan et al. 2003). There are several nano-scale spherical precipitates in the S200 sample with different element content from

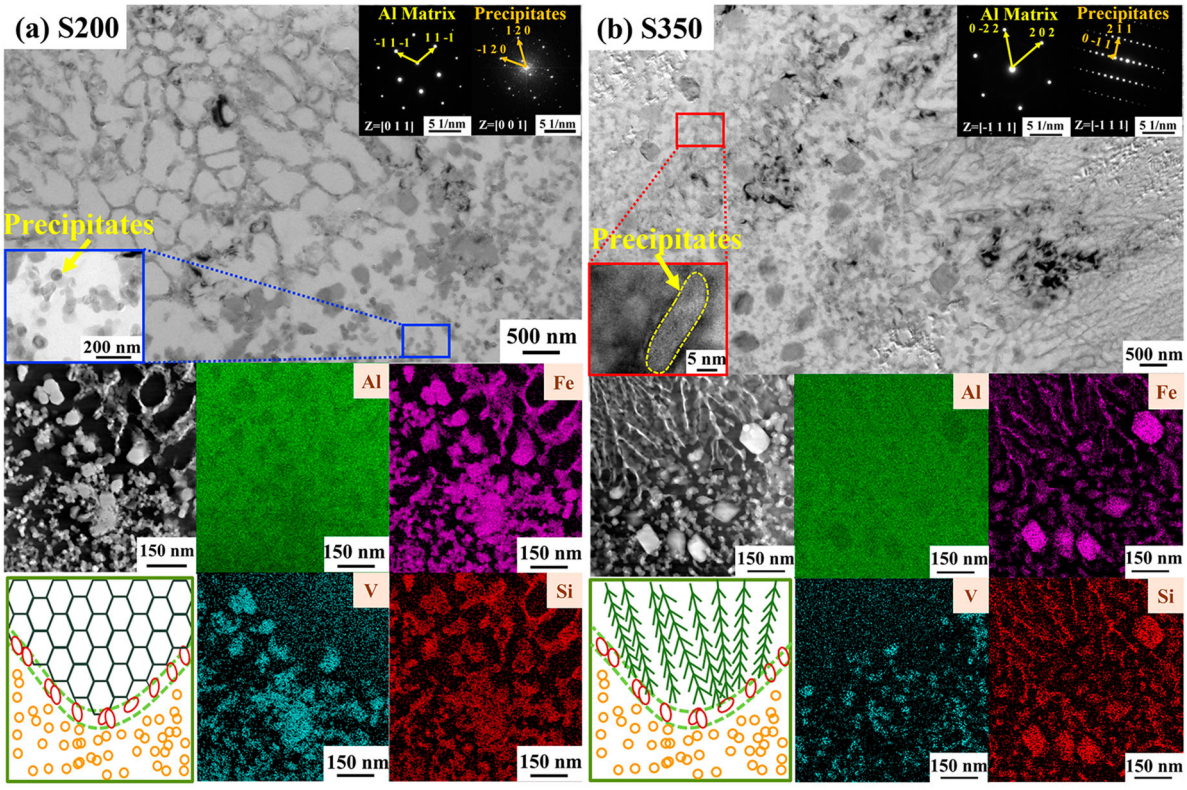

Figure 7. TEM images and corresponding EDS maps at the MPB area in Figure 4 and its corresponding schematic maps: (a) P2, and (b) P4 (inset: HR-STEM images and SAED patterns of the precipitates and Al matrix in each sample).

$Al_{12}(Fe, V)_3Si$ phase in the S350 samples. It is worth mentioning that this phase might be the post cursor phase of $Al_{12}(Fe, V)_3Si$ such as $Al_8(Fe, V)_2Si$ and Al_3Fe due to the lower cooling rate compared to 10^5 K/s (Tan et al. 2003). Furthermore, the structure of this phase also changed from BCC of $Al_{12}(Fe, V)_3Si$ to the hexagonal close-packed (HCP) structure of the $Al_8(Fe, V)_2Si$ (Korchef, Champion, and Njah 2007; Qu et al. 2010). Qualitative EDS analysis with TEM demonstrates that the particles are also enriched in Fe, V, and Si as shown above. Therefore, according to the results given by STEM patterns and EDS analysis, it stimulates the formation of $Al_8(Fe, V)_2Si$ under the S200 parameter. According to the analysis above, the chemical compositions of P1 to P4 are compared in Table 2.

Table 2. The comparison of chemical compositions (wt%) of each position in the MP and MPB area of S200 and S350 samples is shown in Figure 4.

Element (wt%)	Al	Fe	V	Si
P1	85.74	11.44	1.38	1.44
P2-Al Matrix	99.45	0.21	0.19	0.15
P2-Precipitates	70.59	22.07	4.10	3.23
P3	84.42	12.81	1.36	1.41
P4-Al Matrix	98.05	0.61	0.94	0.40
P4-Precipitates	75.36	16.08	4.99	3.57

3.3. Mechanical properties

In order to investigate the micro-mechanical properties of S200 and S350 samples in detail, the nano-hardness from MP area to MPB area of alloys is depicted in Figure 8. The indentations across the MPB area from one MP area to another MP area. The S200 sample has 2.08 GPa in the MP area and dropped down to 1.29 GPa in the MPB area, which results from the high cooling rate in the MP area and heat-treatment effect in the MPB area respectively (Pauly et al. 2018; Wang et al. 2020). Meanwhile, the nano-hardness significantly decreases from the centre of the MP area to the MPB area due to the reduction of the cooling rate along the building direction (Pauly et al. 2018; Dai et al. 2017). The same phenomena are also shown in the S350 sample, which has a nano-hardness of 3.56 GPa in the MP area and 1.99 GPa in the MPB area. The above analyses indicate that the different area of alloys has different micro-mechanical properties, which drives us to consider this difference when discussing the strengthening mechanism and fracture mechanism.

The curves between the relationship of compressive strength and true stress at room temperature and their corresponding deformed morphologies along the building direction are shown in Figure 9(a). The ultimate

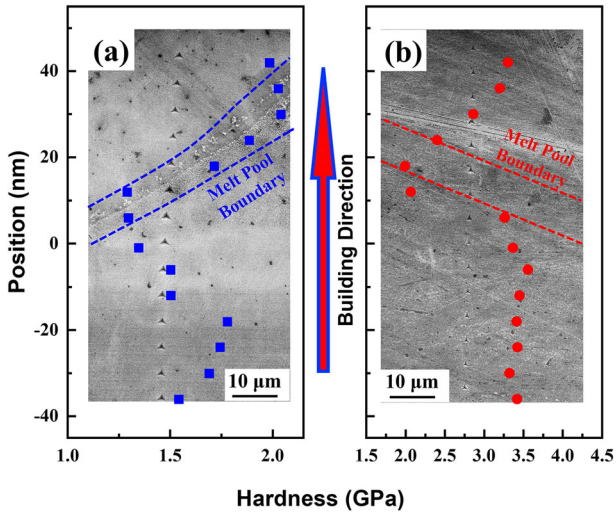

Figure 8. The nano-hardness of LPBF produced AA8009 alloy and their corresponding position in (a) S200 sample and (b) S350 sample.

compressive strength of 550 ± 12 MPa is observed from the LPBF S200 specimens, which did not break up to 40% deformation. Compared with the LPBF S200 samples, the LPBF S350 alloy displays a higher ultimate compressive strength (882 ± 15 MPa) but failed at 34.5 ± 3.3%. It indicates that the difference in processing parameters results in a significant effect on the mechanical properties of LPBF AA8009 alloys, which is a key factor in tailoring the microstructure of LPBF alloys for the synergistic improvement of strengthening-toughening properties.

The cross-sectional fracture surfaces show that the main crack propagation in the fractured S350 sample propagates across the inner of the melt pool, and the cracks are initiated at the edge of the MPB area. The different fracture morphologies indicate the unique failure mechanism. For the S350 sample, although the high nano-hardness of the Al matrix means the α-Al matrix can withstand high stress (Figure 8), the crack would expand rapidly across the alloy under high stress. However, the stress during the loading can only facilitate the crack initiation in the S200 sample with low nano-hardness, where the position with the lowest nano-hardness (Figure 8). To clarify the strengthening mechanism of SLM AA8009 alloy with different parameters, the key strengthening mechanism is considered and discussed comprehensively.

Generally, there are five independent strengthening mechanisms at work in metallic materials (Li et al. 2018), i.e. flow stress, grain refinement strengthening, dislocation strengthening, solid-solution strengthening, and Orowan strengthening (some calls precipitation strengthening) (Chen et al. 2022). Therefore, the yield strength could be simplified as follows:

$$\sigma_{YS} = \sigma_0 + \sigma_{HP} + \sigma_{dis} + \sigma_{ss} + \sigma_{orowan} \quad (8)$$

where σ_0 is the flow stress. The σ_0 values is a common value in Al alloys ($\sigma_0 = 35$ MPa), which is found in Ref. (Shanmugasundaram et al. 2009).

The grain size of α-Al matrix has a significant effect on the strength, which can be estimated by using the Hall-Petch equation (Li et al. 2018; Thangaraju et al. 2012).

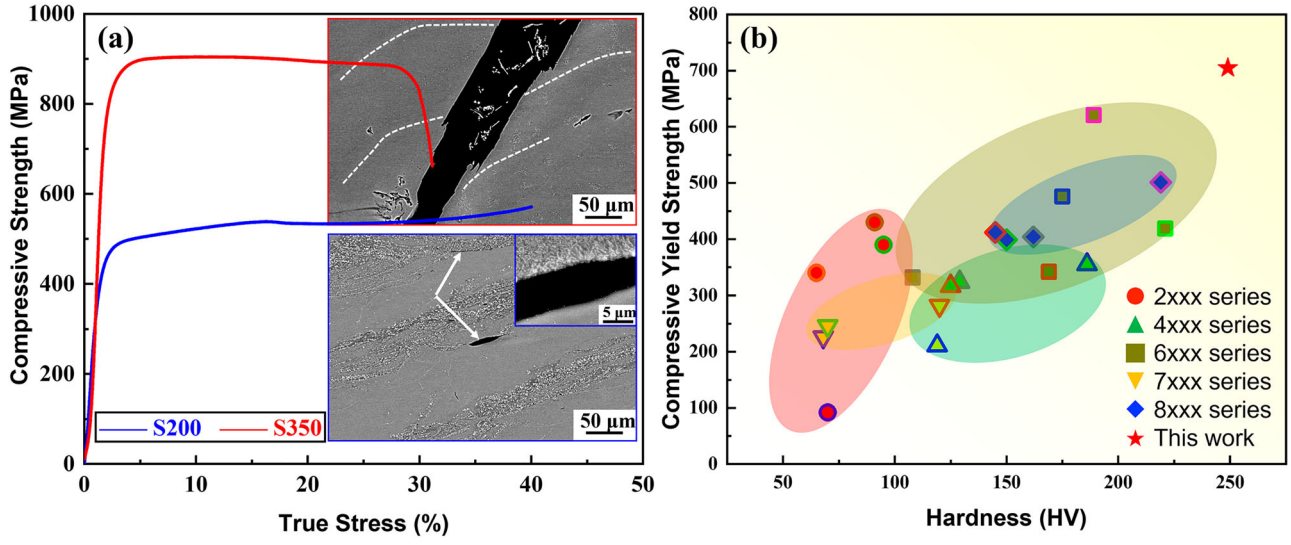

Figure 9. (a) Compressive stress-strain curves and the corresponding fracture morphologies along the building direction of the LPBFed AA8009 alloys after the compression test. (b) Comparison of compressive yield strength and hardness of LPBFed AA8009 alloy with other common Al alloys (Kannan et al. 2020; Sivananthan, Ravi, and Samuel 2020; Tang et al. 2021; Manca et al. 2019; Aboulkhair et al. 2016; de Araujo et al. 2021; Liu et al. 2022; Tang et al. 2021; Lu et al. 2020; Xi et al. 2019).

The grain refinement strengthening of S200 and S350 samples is defined (σ_{HP}) as follows:

$$\sigma_{\mathrm{HP}} = kd^{-1/2} \tag{9}$$

where k is the Hall-Petch coefficient ($k = 0.04$ MPa·m$^{1/2}$) (Hansen 2004), d refers to the grain size ($d_{S200} = 14.3$ μm and $d_{S350} = 16.0$ μm measured in EBSD graphs). Due to the weak effect of heterogeneous microstructure on the grain size of MP and MPB, the σ_{HP} can be calculated directly to be 11 and 10 MPa for S200 and S350 samples, respectively.

However, due to the different heterogeneous microstructure of S200 and S350 samples shown in Figure 4 (c, d), the effect of this heterogeneous microstructure on the mechanical properties has to be considered to ensure an accurate analysis of the strengthening mechanism. Therefore, the dislocation strengthening, Orowan strengthening, and solid solution strengthening of the melt pool area and the melt pool boundary area would be calculated separately.

Geometrically necessary dislocations (GND) are the key factor to estimate the value of dislocation strengthening, which refers to the force required to form plastic deformation. The relationship between dislocation strengthening and GND (ρ_{dis}) can be expressed by the Bailey-Hirsch (or Taylor) relationship as shown (Bailey and Hirsch 1962):

$$\sigma_{dis} = M_{Taylor}\alpha G b \rho_{dis}^{1/2} \tag{10}$$

where M_{Taylor} is set as 3.33 for both the S350 and the S200 samples according to the data from EBSD analysis (Stoller and Zinkle 2000; Hadadzadeh, Amirkhiz, and Mohammadi 2019) that correlates the yield stress to the critical resolved shear stress for polycrystal metals, α is a material-dependent constant (Al = 0.16) (Hadadzadeh, Amirkhiz, and Mohammadi 2019). G is the shear modulus (G = 26.5 GPa) (Hadadzadeh et al. 2019), b is the value of the Burgers vector (b = 0.286 nm) (Miyajima et al. 2010), and ρ_{dis} follows the following equation.

$$\rho_{dis} = \rho_{MP}V_{MP} + \rho_{MPB}V_{MPB} \tag{11}$$

where V is the volume fraction of each zone and ρ_{dis} is GND of each zone, which are mentioned above (Figure 4). Based on equation 11, ρ_{dis} of S200 and S350 are 1.94×10^{14}/m^2 and 1.84×10^{14}/m^2, respectively, thereby and σ_{dis} of S200 and S350 sample is calculated as 56 and 54 MPa.

With the assistance of the high cooling rate during the LPBF process, Fe, Si, and V atoms are diffused into Al-matrix in both samples. The difference in counts, sizes, and shear modulus of solute atoms may cause localised strain fields to impede the movement of dislocations and atoms through the lattice, which is an important way to enhance the yield strength of the material. Due to the contribution of supersaturated atoms to solid solution strengthening, solid solution strengthening could be described as (Li et al. 2022):

$$\sigma_{SS} = M_{Taylor}\left(\frac{3}{8}\right)^{\frac{2}{3}}\left(\frac{1+v}{1-v}\right)^{\frac{4}{3}}\left(\frac{w}{b}\right)^{\frac{1}{3}}G|\varepsilon|^{\frac{4}{3}}c^{\frac{2}{3}} \tag{12}$$

where M_{Taylor} is set as 3.33 and G refers to the shear modulus, v represents the Poisson's ratio of Al (0.345), w = 5b (b: the magnitude of the Burgers vector), ε is the lattice misfit strain (4.6 for Fe, 0.87 for Si and 3.11 for V) (Li et al. 2022; Michi et al. 2022). c is the mean concentrations of the various solute atoms from the TEM/EDS results, which is calculated by the following equation:

$$c = c_{MP}V_{MP} + c_{MPB}V_{MPB} \tag{13}$$

According to the proportion of supersaturated atoms in the MP and the MPB areas of the S200 and the S350 samples (Table 2), the estimated strength increment caused by solid solution strengthening is 317 MPa for the S200 sample and 375 MPa for the S350 sample.

Based on the classical strengthening mechanism, Orowan strengthening is caused by either dislocation looping of the coarser semi-coherent particles or dislocation shearing in the case of fine coherent particles. As shown in Figure 6, there is no presence of the secondary phase in the MP area, indicating that no Orowan strengthening exists in the MP area. The strength increment contributed by dislocation looping in the MPB area could be described as (Li et al. 2021; Nie et al. 2018):

$$\sigma_{orowan} = \frac{0.4MGb}{\pi L}\frac{\ln\frac{r\pi}{2b}}{\sqrt{1-v}} \tag{14}$$

where $L = r\sqrt{\left(\frac{2\pi}{3f} - \frac{\pi}{2}\right)}$, r is the mean particle radius, and f refers to the volume fraction of secondary phases in the melt pool boundary area. The particle size in the S200 sample is 33 nm observed in Figure 7 (a) and 5 nm for the S350 sample shown in Figure 7 (b) measured by Image-Pro Plus software, which can contribute to 93 and 243 MPa for each of the samples at the MPB area according to Eq. (14).

According to the discussion and calculation on the strength increment, the comparison chart on the measured and calculated yield strength of S200 and S350 samples is displayed in Figure 10. The calculated theoretical yield strength of the S200 sample is 511 MPa, which is 34% higher than the measured

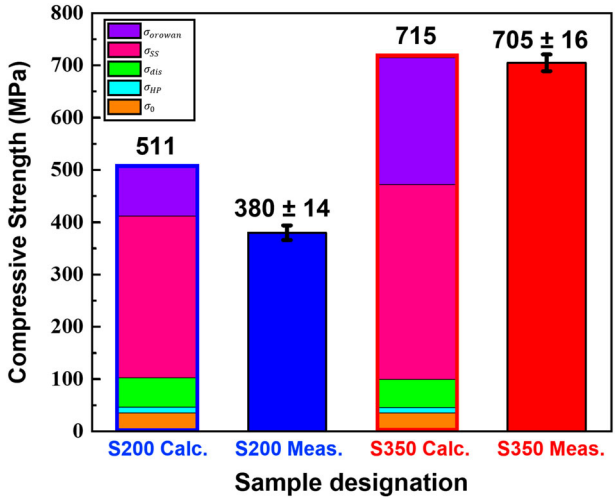

Figure 10. The measured CYS and individual contributions of different strengthening mechanisms to the theoretical strength of the S200 and S350 samples.

value, it shows that the measured experimental yield strength is roughly in accordance with the calculated value. The difference between calculated theoretical yield strength and measured value may result from the accuracy of instrument calibrations and some potentially interacting between these mechanisms (Cao et al. 2017). While the calculated value of S350 was 715 MPa, almost identical to the measured compression yield strength, indicating the measured result of S350 is also close to the calculated value.

4. Conclusions

In this work, fully dense Al-8.3Fe-1.3V-1.8Si alloy (AA8009) was successfully fabricated by LPBF. Two fully dense samples (S200: laser power of 200 W and scanning speed of 300 mm/s; and S350: laser power of 350 W and scanning speed of 1200 mm/s) show a different heterogeneous microstructure resulting in a significant difference of mechanical behaviour, which paves a way to design LPBFed AA8009 components with suitable mechanical properties.

(1) S200 alloy has a combined morphology with a fan-shaped structure and horizontal structure while S350 only shows a wider and deeper fan-shaped morphology. The different alloys have different volume fractions of melt pool (MP) area and melt pool boundary (MPB) area, which area have their unique microstructure.
(2) Both alloys have columnar grains of similar sizes (average columnar grain of 14.3 μm for S200; average columnar grain of 16.0 μm for S350), but they show different values in MP area and the MPB, where LPBFed S350 sample has fewer dislocations than S200 sample.
(3) There are no secondary particles in the MP area of both alloys, where only supersaturated Fe, V, and Si atoms exist in the Al matrix. However, S200 alloy has cellular structure composed of $Al_8(Fe, V)_2Si$ phase in the MPB area, and dendritic structure composed of $Al_{12}(Fe, V)_3Si$ exists in the MPB area of S350. Meanwhile, the supersaturated content of every atom in S350 samples is higher than those in S200.
(4) The solid-solution strengthening and Orowan strengthening is the main strengthening mechanism for the excellent strength of LPBFed AA8009 alloys, and the Orowan strengthening is the key factor to enhance S350 samples with a higher CYS (705 ± 16 MPa) than S200 (380 ± 14 MPa).
(5) Due to the different nano-hardness of their heterogeneous microstructure (S350: 3.56 GPa at MP, 1.99 GPa at MPB; S200: 2.08 GPa at MP, 1.29 GPa at MPB), the two alloys show different failure modes. The main crack propagation in the fractured S350 sample transports across the inner of the melt pool with the failure strain of 34.5 ± 3.3%, while the formation of crack initiation between the MP and MPB area in the S200 sample cannot propagate across the inner melt pool resulting in its better ductility.

Acknowledgements

The authors acknowledge the technical assistance from and fruitful discussion with X. H. Gao, M. H. Li, G.Y. Zheng, and X. Zhang, and the assistance on HRTEM observations from the Electron Microscope Centre of Shenzhen University.

Disclosure statement

No potential conflict of interest was reported by the author(s).

Funding

This work was supported by National Natural Science Foundation of China: [Grant Number 52105385, 52005340]; Shenzhen International Cooperation Research: [Grant Number GJHZ20190822095418365]; NTUT-SZU Joint Research Program: [Grant Number 2022010,NTUT-SZU-111-04]; Guangdong Basic and Applied Basic Research Foundation: [Grant Number 2020A1515110869,2022A1515010781].

Notes on contributors

S.J. Yu is a postgraduate of mechanical engineering at Shenzhen University.

P. Wang is an assistant professor at Shenzhen University. He holds a Ph.D. from IFW Dresden/TU Dresden. His research topics include additive manufacturing of advanced materials (high-performance alloys, high-temperature ceramics, and their composites), and processing-structure-property relationships of AMed materials. He has been listed as Stanford World Top 2% Scientist for the years 2021 and 2022.

H.C. Li is an associate professor of Shanghai University of Engineering Science.

Prof R. Setchi FIET, FIMechE, FBCS, SMIEEE has a distinguished track record of research in additive manufacturing (AM), including multi-material, AI / Industry 4.0 and sustainable manufacturing. She is Professor of High-Value Manufacturing and the Founding Director of the Centre for AI, Robotics and Human-Machine Systems (IROHMS) at Cardiff. Over a period of 20 years, Professor Setchi has contributed over 260 peer reviewed publications including 14 books and over 100 journal articles and secured external grant support totalling more than £25 million. She has collaborated with over 20 UK and 30 overseas universities, 15 research organisations and 30 industrial companies from more than 20 countries in Europe, Asia and Australia. She has provided research leadership on over 30 collaborative projects funded by UK and overseas funding bodies, including Royal Society, Royal Academy of Engineering, EPSRC and the European Commission. In the area of additive manufacturing, she has completed research projects with many UK-based companies including Airbus, Continental Teves, Qioptiq, Renishaw and Sandvik Osprey. She is Associate Editor/member of the Editorial Board of several international journals.

M.W. Wu is a professor of National Taipei University of Technology.

Z.Y. Liu is a distinguished research fellow in Shenzhen University. His research covers additive manufacturing of advanced metallic materials including high entropy alloys, high-strength steel, and metallic glasses, and strengthening and toughening mechanisms of the alloys.

Z.W. Chen is currently a tenured Professor and the Director of the Additive Manufacturing Institute at Shenzhen University. His research covers the additive manufacturing of high-performance materials for advanced applications. He has been elected as Fellow of the International Association of Advanced Materials (IAAM) and listed as Stanford World Top 2% Scientist for the year 2021 and 2022.

S. Waqar is an Assistant Professor in Institute of Space Technology, Pakistan. His research interests are Metal 3D Printing, Modeling and Simulation of Metal 3D printing and Functionally Graded Meta Materials.

L.C. Zhang is a Professor of Materials Engineering and the Program Leader–Mechanical Engineering in the School of Engineering at Edith Cowan University. His current research interests focus on the metal additive manufacturing (e.g. selective laser melting, electron beam melting), titanium alloys and composites, and processing-microstructure-properties in high-performance materials.

ORCID

P. Wang http://orcid.org/0000-0002-4141-0511
R. Setchi http://orcid.org/0000-0002-7207-6544

References

Aboulkhair, Nesma T., Ian Maskery, Chris Tuck, Ian Ashcroft, and Nicola M. Everitt. 2016. "The Microstructure and Mechanical Properties of Selectively Laser Melted AlSi10Mg: The Effect of a Conventional T6-Like Heat Treatment." *Materials Science and Engineering: A*, doi:10.1016/j.msea.2016.04.092.

Attar, Hooyar, Matthias Bönisch, Mariana Calin, L. C. Zhang, Sergio Scudino, and Jürgen Eckert. 2014a. "Selective Laser Melting of in Situ Titanium-Titanium Boride Composites: Processing, Microstructure and Mechanical Properties." *Acta Materialia* 76: 13–22. doi:10.1016/j.actamat.2014.05.022.

Attar, H., M. Calin, L. C. Zhang, S. Scudino, and J. Eckert. 2014b. "Manufacture by Selective Laser Melting and Mechanical Behavior of Commercially Pure Titanium." *Materials Science and Engineering: A* 593: 170–177. doi:10.1016/j.msea.2013.11.038.

Attar, H., K. G. Prashanth, A. K. Chaubey, M. Calin, L. C. Zhang, S. Scudino, and J. Eckert. 2015. "Comparison of Wear Properties of Commercially Pure Titanium Prepared by Selective Laser Melting and Casting Processes." *Materials Letters* 142: 38–41. doi:10.1016/j.matlet.2014.11.156.

Bailey, J. E., and Peter Bernhard Hirsch. 1962. "The Recrystallization Process in Some Polycrystalline Metals." *Proceedings of the Royal Society of London. Series A. Mathematical and Physical Sciences* 267 (1328): 11–30.

Bois-Brochu, Alexandre, Carl Blais, Franck Armel Tchitembo Goma, Daniel Larouche, Julien Boselli, and Mathieu Brochu. 2014. "Characterization of Al-Li 2099 Extrusions and the Influence of Fiber Texture on the Anisotropy of Static Mechanical Properties." *Materials Science and Engineering: A* 597: 62–69. doi:10.1016/j.msea.2013.12.060.

Bouabbou, Abdelkrim, and Sebastien Vaudreuil. 2022. "Understanding Laser-Metal Interaction in Selective Laser Melting Additive Manufacturing Through Numerical Modelling and Simulation: A Review." *Virtual and Physical Prototyping* 17 (3): 543–562. doi:10.1080/17452759.2022.2052488.

Cacace, Stefania, and Quirico Semeraro. 2021. "Fast Optimisation Procedure for the Selection of L-PBF Parameters Based on Utility Function." *Virtual and Physical Prototyping* 17 (2): 125–137. doi:10.1080/17452759.2021.1998871.

Cao, B., M. Shaeffer, D. Cadel, K. T. Ramesh, and S. Prasad. 2017. "An Analysis of Strengthening Mechanisms and Rate-Dependence in a High Strength Aluminum Alloy." *Journal of Dynamic Behavior of Materials* 4 (1): 6–17. doi:10.1007/s40870-017-0136-0.

Carreño, F., M. T. Pérez-Prado, G. González-Doncel, and O. A. Ruano. 1998. "Texture Stability of a Rapidly Solidified Dispersion Strengthened Al-Fe-V-Si Material." *Scripta Materialia* 38 (9): 1427–1433. doi:10.1016/s1359-6462(98)00039-6.

Chen, Liangyu, Shunxing Liang, Yujing Liu, and Laichang Zhang. 2021. "Additive Manufacturing of Metallic Lattice Structures: Unconstrained Design, Accurate Fabrication, Fascinated Performances, and Challenges." *Materials Science and Engineering: R: Reports* 146, doi:10.1016/j.mser.2021.100648.

Chen, Kai, Lihua Zhan, Yongqian Xu, Bolin Ma, Quanqing Zeng, and Shugen Luo. 2022. "Optimizing Strength and Ductility in

7150 Al Alloys via Rapid Electropulsing Cyclic Heat Treatment." *Journal of Alloys and Compounds* 903, doi:10.1016/j.jallcom.2022.163985.

Dai, Donghua, Dongdong Gu, Reinhart Poprawe, and Mujian Xia. 2017. "Influence of Additive Multilayer Feature on Thermodynamics, Stress and Microstructure Development During Laser 3D Printing of Aluminum-Based Material." *Science Bulletin* 62 (11): 779–787. doi:10.1016/j.scib.2017.05.007.

de Araujo, Aylanna P. M., Simon Pauly, Rodolfo L. Batalha, Francisco G. Coury, Claudio S. Kiminami, Volker Uhlenwinkel, and Piter Gargarella. 2021. "Additive Manufacturing of a Quasicrystal-Forming Al95Fe2Cr2Ti1 Alloy with Remarkable High-Temperature Strength and Ductility." *Additive Manufacturing* 41, doi:10.1016/j.addma.2021.101960.

Deng, Junwang, Chao Chen, Xiaochun Liu, Yunping Li, Kechao Zhou, and Shengmin Guo. 2021. "A High-Strength Heat-Resistant Al-5.7Ni Eutectic Alloy with Spherical Al3Ni Nano-Particles by Selective Laser Melting." *Scripta Materialia* 203, doi:10.1016/j.scriptamat.2021.114034.

Deng, P. Y., K. K. Wang, J. Y. Du, and H. J. Wu. 2020. "From Dislocation to Nano-Precipitation: Evolution to Low Thermal Conductivity and High Thermoelectric Performance in n-Type PbTe." *Advanced Functional Materials* 30 (49), doi:10.1002/adfm.202005479.

Didier, P., G. Le Coz, G. Robin, P. Lohmuller, B. Piotrowski, A. Moufki, and P. Laheurte. 2021. "Consideration of SLM Additive Manufacturing Supports on the Stability of Flexible Structures in Finish Milling." *Journal of Manufacturing Processes* 62: 213–220. doi:10.1016/j.jmapro.2020.12.027.

Franck, R. E., and J. A. Hawk. 1989. "Effect of Very High Temperatures on the Mechanical Properties of Al-Fe-V-Si Alloy." *Scripta Metallurgica* 23 (1): 113–118. doi:10.1016/0036-9748(89)90103-8.

Gilman, P., M. Zedalis, J. Peltier, and S. Das. 1988. "Rapidly Solidified Aluminum-Transition Metal Alloys for Aerospace Applications" Proceedings of Aircraft Design, Systems and Operations Conference, September, p. 4444. https://doi.org/10.2514/6.1988-4444.

Goyal, Gagan K., Shriparna Mukherjee, Ramesh C. Mallik, Satish Vitta, Indradev Samajdar, and Titas Dasgupta. 2019. "High Thermoelectric Performance in Mg2(Si0.3Sn0.7) by Enhanced Phonon Scattering." *ACS Applied Energy Materials* 2 (3): 2129–2137. doi:10.1021/acsaem.8b02148.

Gu, Dongdong, Fei Chang, and Donghua Dai. 2014. "Selective Laser Melting Additive Manufacturing of Novel Aluminum Based Composites with Multiple Reinforcing Phases." *Journal of Manufacturing Science and Engineering* 137 (2): 021010. doi:10.1115/1.4028925.

Gustmann, T., A. Neves, U. Kühn, P. Gargarella, C. S. Kiminami, C. Bolfarini, J. Eckert, and S. Pauly. 2016. "Influence of Processing Parameters on the Fabrication of a Cu-Al-Ni-Mn Shape-Memory Alloy by Selective Laser Melting." *Additive Manufacturing* 11: 23–31. doi:10.1016/j.addma.2016.04.003.

Hadadzadeh, Amir, Babak Shalchi Amirkhiz, and Mohsen Mohammadi. 2019a. "Contribution of Mg2Si Precipitates to the Strength of Direct Metal Laser Sintered AlSi10Mg." *Materials Science and Engineering: A* 739: 295–300. doi:10.1016/j.msea.2018.10.055.

Hadadzadeh, Amir, Babak Shalchi Amirkhiz, Akindele Odeshi, Jian Li, and Mohsen Mohammadi. 2019b. "Role of Hierarchical Microstructure of Additively Manufactured AlSi10Mg on Dynamic Loading Behavior." *Additive Manufacturing* 28: 1–13. doi:10.1016/j.addma.2019.04.012.

Hansen, Niels. 2004. "Hall-Petch Relation and Boundary Strengthening." *Scripta Materialia* 51 (8): 801–806. doi:10.1016/j.scriptamat.2004.06.002.

Hooper, Paul A. 2018. "Melt Pool Temperature and Cooling Rates in Laser Powder bed Fusion." *Additive Manufacturing* 22: 548–559. doi:10.1016/j.addma.2018.05.032.

Huang, B., K. N. Ishihara, and P. H. Shingu. 1997. "Metastable Phases of Al-Fe System by Mechanical Alloying." *Materials Science and Engineering: A* 231 (1-2): 72–79.

Kannan, C. Senthamarai, S. Sai Sree Chandra, G. Punith Krishnan, and S. Pravin Raj. 2020. "A Review on Additive Manufacturing of AA2024 and AA6061 Alloys Using Powder bed Fusion." Paper presented at the IOP conference series: materials science and engineering.

Koh, H. K., J. G. S. Moo, S. L. Sing, and W. Y. Yeong. 2022. "Use of Fumed Silica Nanostructured Additives in Selective Laser Melting and Fabrication of Steel Matrix Nanocomposites." *Materials (Basel)* 15 (5), doi:10.3390/ma15051869.

Koo, H. H., and W. A. Baeslack. 1992. "Structure,: Properties, and Fracture of Linear Friction Welded Al-Fe-V-Si Alloy 8009." *Materials Characterization* 28 (2): 157–164. doi:10.1016/1044-5803(92)90039-k.

Korchef, Atef, Yannick Champion, and Nabil Njah. 2007. "X-ray Diffraction Analysis of Aluminium Containing Al8Fe2Si Processed by Equal Channel Angular Pressing." *Journal of Alloys and Compounds* 427 (1-2): 176–182. doi:10.1016/j.jallcom.2006.03.010.

Kou, Sindo. 2015. "A Criterion for Cracking During Solidification." *Acta Materialia* 88: 366–374. doi:10.1016/j.actamat.2015.01.034.

Koutny, Daniel, Daniel Skulina, Libor Pantělejev, David Paloušek, Blanka Lenczowski, Frank Palm, and Andreas Nick. 2018. "Processing of Al-Sc Aluminum Alloy Using SLM Technology." *Procedia CIRP* 74: 44–48. doi:10.1016/j.procir.2018.08.027.

Li, Guichuan, Etienne Brodu, Jeroen Soete, Huiliang Wei, Tingting Liu, Tao Yang, Wenhe Liao, and Kim Vanmeensel. 2021. "Exploiting the Rapid Solidification Potential of Laser Powder bed Fusion in High Strength and Crack-Free Al-Cu-Mg-Mn-Zr Alloys." *Additive Manufacturing* 47, doi:10.1016/j.addma.2021.102210.

Li, Rui, Jiapeng Hou, Wenhao Yang, Hongyun Yu, Qiang Wang, and Zhefeng Zhang. 2018. "Strengthening Mechanism and Yield Strength Prediction of Cold-Drawn Commercially Pure Aluminum Wire." Paper presented at the IOP conference series: materials science and engineering.

Li, Qiuge, Guichuan Li, Xin Lin, Daiman Zhu, Jinhang Jiang, Shuoqing Shi, Fenggang Liu, Weidong Huang, and Kim Vanmeensel. 2022. "Development of a High Strength Zr/Sc/Hf-Modified Al-Mn-Mg Alloy Using Laser Powder Bed Fusion: Design of a Heterogeneous Microstructure Incorporating Synergistic Multiple Strengthening Mechanisms." *Additive Manufacturing* 57, doi:10.1016/j.addma.2022.102967.

Li, P. Y., H. J. Yu, S. C. Chai, and Y. R. Li. 2003. "Microstructure and Properties of Rapidly Solidified Powder Metallurgy Al-

Fe-Mo-Si Alloys." *Scripta Materialia* 49 (9): 819–824. doi:10.1016/s1359-6462(03)00483-4.

Lienert, T. J., P. B. Nagy, and W. A. Baeslack. 1998. "Ultrasonic Characterization of Microstructures in Inertia Friction Welds on SiC-Reinforced 8009 Aluminum." *Welding Journal-New York* 77: 14-s.

Liu, Y. J., Z. Liu, Y. Jiang, G. W. Wang, Y. Yang, and L. C. Zhang. 2018a. "Gradient in Microstructure and Mechanical Property of Selective Laser Melted AlSi10Mg." *Journal of Alloys and Compounds* 735: 1414–1421. doi:10.1016/j.jallcom.2017.11.020.

Liu, Tong, Qianqian Wang, Xiaoye Cai, Lu Pan, Jiansheng Li, Ze Zong, Zonghui Cheng, Zongjun Tian, Liangshun Luo, and Yanqing Su. 2022. "Effect of Laser Power on Microstructures and Properties of Al-4.82Mg-0.75Sc-0.49Mn-0.28Zr Alloy Fabricated by Selective Laser Melting." *Journal of Materials Research and Technology* 18: 3612–3625. doi:10.1016/j.jmrt.2022.03.162.

Liu, Shiwen, Haihong Zhu, Gangyong Peng, Jie Yin, and Xiaoyan Zeng. 2018b. "Microstructure Prediction of Selective Laser Melting AlSi10Mg Using Finite Element Analysis." *Materials & Design* 142: 319–328. doi:10.1016/j.matdes.2018.01.022.

Lu, J. L., X. Lin, H. L. Liao, N. Kang, W. D. Huang, and C. Coddet. 2020. "Compression Behaviour of Quasicrystal/Al Composite with Powder Mixture Driven Layered Microstructure Prepared by Selective Laser Melting." *Optics & Laser Technology* 129, doi:10.1016/j.optlastec.2020.106277.

Manca, Dario Rafael, A. Yu Churyumov, A. V. Pozdniakov, D. K. Ryabov, V. A. Korolev, and D. K. Daubarayte. 2019. "Novel Heat-Resistant Al-Si-Ni-Fe Alloy Manufactured by Selective Laser Melting." *Materials Letters* 236: 676–679. doi:10.1016/j.matlet.2018.11.033.

Michi, Richard A., Alex Plotkowski, Amit Shyam, Ryan R. Dehoff, and Sudarsanam Suresh Babu. 2022. "Towards High-Temperature Applications of Aluminium Alloys Enabled by Additive Manufacturing." *International Materials Reviews* 67 (3): 298–345. doi:10.1080/09506608.2021.1951580.

Miyajima, Yoji, Masatoshi Mitsuhara, Satoshi Hata, Hideharu Nakashima, and Nobuhiro Tsuji. 2010. "Quantification of Internal Dislocation Density Using Scanning Transmission Electron Microscopy in Ultrafine Grained Pure Aluminium Fabricated by Severe Plastic Deformation." *Materials Science and Engineering: A* 528 (2): 776–779. doi:10.1016/j.msea.2010.09.058.

Nie, Xiaojia, Hu Zhang, Haihong Zhu, Zhiheng Hu, Linda Ke, and Xiaoyan Zeng. 2018. "Effect of Zr Content on Formability, Microstructure and Mechanical Properties of Selective Laser Melted Zr Modified Al-4.24Cu-1.97Mg-0.56Mn Alloys." *Journal of Alloys and Compounds* 764: 977–986. doi:10.1016/j.jallcom.2018.06.032.

Nouri, Z., R. Taghiabadi, and M. Moazami-Goudarzi. 2020. "Mechanical Properties Enhancement of Cast Al-8.5Fe-1.3V-1.7Si (FVS0812) Alloy by Friction Stir Processing." *Archives of Civil and Mechanical Engineering* 20 (4), doi:10.1007/s43452-020-00106-1.

Pauly, Simon, Lukas Löber, Romy Petters, Mihai Stoica, Sergio Scudino, Uta Kühn, and Jürgen Eckert. 2013. "Processing Metallic Glasses by Selective Laser Melting." *Materials Today* 16 (1-2): 37–41. doi:10.1016/j.mattod.2013.01.018.

Pauly, Simon, Pei Wang, Uta Kühn, and Konrad Kosiba. 2018. "Experimental Determination of Cooling Rates in Selectively Laser-Melted Eutectic Al-33Cu." *Additive Manufacturing* 22: 753–757. doi:10.1016/j.addma.2018.05.034.

Prasetya, Ahadi Damar, Mujamilah Muhammad Rifai, and Hiroyuki Miyamoto. 2020. "X-ray Diffraction (XRD) Profile Analysis of Pure ECAP-Annealing Nickel Samples." *Journal of Physics: Conference Series* 1436 (1): 012113. doi:10.1088/1742-6596/1436/1/012113.

Prashanth, K. G., S. Scudino, and J. Eckert. 2017. "Defining the Tensile Properties of Al-12Si Parts Produced by Selective Laser Melting." *Acta Materialia* 126: 25–35. doi:10.1016/j.actamat.2016.12.044.

Qu, Hua, Weidong Liu, Gang Zhou, Xiaolu Shen, and Chuang Liu. 2010. "Study on the Precipitated Behavior and Stability of the Strengthening Phase Al12(Fe,X)3Si in Al-Fe-Si-X Alloys with the EET Theory." *Advanced Materials Research* 152-153: 743–747. doi:10.4028/www.scientific.net/AMR.

Ravi, C. 2004. "First-principles Study of Crystal Structure and Stability of Al-Mg-Si-(Cu) Precipitates." *Acta Materialia* 52 (14): 4213–4227. doi:10.1016/j.actamat.2004.05.037.

Saboori, Abdollah, Alberta Aversa, Giulio Marchese, Sara Biamino, Mariangela Lombardi, and Paolo Fino. 2020. "Microstructure and Mechanical Properties of AISI 316L Produced by Directed Energy Deposition-Based Additive Manufacturing: A Review." *Applied Sciences* 10 (9), doi:10.3390/app10093310.

Sahoo, K. L., C. S. Sivaramakrishnan, and A. K. Chakrabarti. 2000. "Solidification Characteristics of the Al-8.3Fe-0.8V-0.9Si Alloy." *Metallurgical and Materials Transactions a-Physical Metallurgy and Materials Science* 31 (6): 1599–1610.

Shanmugasundaram, T., M. Heilmaier, B. S. Murty, and V. Subramanya Sarma. 2009. "Microstructure and Mechanical Properties of Nanostructured Al-4Cu Alloy Produced by Mechanical Alloying and Vacuum Hot Pressing." *Metallurgical and Materials Transactions A* 40 (12): 2798–2801. doi:10.1007/s11661-009-0005-0.

Sing, S. L. 2022. "Perspectives on Additive Manufacturing Enabled Beta-Titanium Alloys for Biomedical Applications." *Int J Bioprint* 8 (1): 478. doi:10.18063/ijb.v8i1.478.

Sing, S. L., C. N. Kuo, C. T. Shih, C. C. Ho, and C. K. Chua. 2021. "Perspectives of Using Machine Learning in Laser Powder bed Fusion for Metal Additive Manufacturing." *Virtual and Physical Prototyping* 16 (3): 372–386. doi:10.1080/17452759.2021.1944229.

Sivananthan, S., K. Ravi, and C. Samson Jerold Samuel. 2020. "Effect of SiC Particles Reinforcement on Mechanical Properties of Aluminium 6061 Alloy Processed Using Stir Casting Route." *Materials Today: Proceedings* 21: 968–970. doi:10.1016/j.matpr.2019.09.068.

Skinner, D. J., R. L. Bye, D. Raybould, and A. M. Brown. 1986. "Dispersion Strengthened Al-Fe-V-Si Alloys." *Scripta Metallurgica* 20 (6): 867–872. doi:10.1016/0036-9748(86)90456-4.

Srivastava, A. K., S. N. Ojha, and S. Ranganathan. 1998. "Microstructural Features and Heat Flow Analysis of Atomized and Spray-Formed Al-Fe-V-Si Alloy." *Metallurgical and Materials Transactions A* 29 (8): 2205–2219. doi:10.1007/s11661-998-0045-x.

Stoller, R. E., and S. J. Zinkle. 2000. "On the Relationship between Uniaxial Yield Strength and Resolved Shear Stress in Polycrystalline Materials." *Journal of Nuclear Materials* 283: 349–352.

Sun, Jingjia, Meng Guo, Keyu Shi, and Dongdong Gu. 2022. "Influence of Powder Morphology on Laser Absorption Behavior and Printability of Nanoparticle-Coated 90W-Ni-Fe Powder During Laser Powder bed Fusion." *Materials Science in Additive Manufacturing* 1 (2), doi:10.18063/msam.v1i2.11.

Sun, Shaobo, Lijing Zheng, Yingying Liu, Jinhui Liu, and Hu Zhang. 2015a. "Characterization of Al-Fe-V-Si Heat-Resistant Aluminum Alloy Components Fabricated by Selective Laser Melting." *Journal of Materials Research* 30 (10): 1661–1669. doi:10.1557/jmr.2015.110.

Sun, Shaobo, Lijing Zheng, Yingying Liu, Jinhui Liu, and Hu Zhang. 2015b. "Selective Laser Melting of Al-Fe-V-Si Heat-Resistant Aluminum Alloy Powder: Modeling and Experiments." *The International Journal of Advanced Manufacturing Technology* 80 (9-12): 1787–1797. doi:10.1007/s00170-015-7137-8.

Sun, Shaobo, Lijing Zheng, Jinhui Liu, and Hu Zhang. 2017. "Microstructure, Cracking Behavior and Control of Al-Fe-V-Si Alloy Produced by Selective Laser Melting." *Rare Metals*, doi:10.1007/s12598-016-0846-9.

Sun, Shaobo, Lijing Zheng, Hui Peng, and Hu Zhang. 2016. "Microstructure and Mechanical Properties of Al-Fe-V-Si Aluminum Alloy Produced by Electron Beam Melting." *Materials Science and Engineering: A* 659: 207–214. doi:10.1016/j.msea.2016.02.053.

Sunagawa, Ichiro. 1999. "Growth and Morphology of Crystals." *Forma-Tokyo* 14 (1/2): 147–166.

Tan, Dunqiang, Wenxian Li, Yude Xiao, Richu Wang, Zhengqing Ma, Baiqing Xiong, Baohong Zhu, and Yongan Zhang. 2003. "Phase Transition of Al-Fe-V-Si Heat-Resistant Alloy by Spray Deposition." *Transactions of Nonferrous Metals Society of China* 13 (3): 568–573.

Tan, Qiyang, Yingang Liu, Zhiqi Fan, Jingqi Zhang, Yu Yin, and Ming-Xing Zhang. 2020. "Effect of Processing Parameters on the Densification of an Additively Manufactured 2024 Al Alloy." *Journal of Materials Science & Technology* 58: 34–45. doi:10.1016/j.jmst.2020.03.070.

Tang, Hao, Yaoxiang Geng, Shunuo Bian, Junhua Xu, and Zhijie Zhang. 2021a. "An Ultra-High Strength Over 700 MPa in Al-Mn-Mg-Sc-Zr Alloy Fabricated by Selective Laser Melting." *Acta Metallurgica Sinica (English Letters)* 35 (3): 466–474. doi:10.1007/s40195-021-01286-2.

Tang, Hao, Yaoxiang Geng, Jinjie Luo, Junhua Xu, Hongbo Ju, and Lihua Yu. 2021b. "Mechanical Properties of High Mg-Content Al-Mg-Sc-Zr Alloy Fabricated by Selective Laser Melting." *Metals and Materials International* 27 (8): 2592–2599. doi:10.1007/s12540-020-00907-2.

Tang, Yiping, Dunqiang Tan, Wenxian Li, Zhijun Pan, Lei Liu, and Wenbin Hu. 2007. "Preparation of Al-Fe-V-Si Alloy by Spray co-Deposition with Added its Over-Sprayed Powders." *Journal of Alloys and Compounds* 439 (1-2): 103–108. doi:10.1016/j.jallcom.2006.08.233.

Thangaraju, Shanmugasundaram, Martin Heilmaier, Budaraju Srinivasa Murty, and Subramanya Sarma Vadlamani. 2012. "On the Estimation of True Hall-Petch Constants and Their Role on the Superposition Law Exponent in Al Alloys." *Advanced Engineering Materials* 14 (10): 892–897. doi:10.1002/adem.201200114.

Uesugi, Tokuteru, and Kenji Higashi. 2013. "First-principles Studies on Lattice Constants and Local Lattice Distortions in Solid Solution Aluminum Alloys." *Computational Materials Science* 67: 1–10. doi:10.1016/j.commatsci.2012.08.037.

Wang, Pei, Fenghua Chen, J. Eckert, S. Pilz, S. Scudino, and K. G. Prashanth. 2021a. "Microstructural Evolution and Mechanical Properties of Selective Laser Melted Ti-6Al-4 V Induced by Annealing Treatment." *Journal of Central South University* 28 (4): 1068–1077. doi:10.1007/s11771-021-4680-3.

Wang, P., L. Deng, K. G. Prashanth, S. Pauly, J. Eckert, and S. Scudino. 2018a. "Microstructure and Mechanical Properties of Al-Cu Alloys Fabricated by Selective Laser Melting of Powder Mixtures." *Journal of Alloys and Compounds* 735: 2263–2266. doi:10.1016/j.jallcom.2017.10.168.

Wang, Pei, Jürgen Eckert, Konda gokuldoss Prashanth, Ming wei Wu, Ivan Kaban, Li xia Xi, and Sergio Scudino. 2020. "A Review of Particulate-Reinforced Aluminum Matrix Composites Fabricated by Selective Laser Melting." *Transactions of Nonferrous Metals Society of China* 30 (8): 2001–2034. doi:10.1016/s1003-6326(20)65357-2.

Wang, Pei, Christoph Gammer, Florian Brenne, Konda Gokuldoss Prashanth, Rafael Gregorio Mendes, Mark Hermann Rümmeli, Thomas Gemming, Jürgen Eckert, and Sergio Scudino. 2018b. "Microstructure and Mechanical Properties of a Heat-Treatable Al-3.5Cu-1.5Mg-1Si Alloy Produced by Selective Laser Melting." *Materials Science and Engineering: A* 711: 562–570. doi:10.1016/j.msea.2017.11.063.

Wang, P., H. C. Li, K. G. Prashanth, J. Eckert, and S. Scudino. 2017. "Selective Laser Melting of Al-Zn-Mg-Cu: Heat Treatment,: Microstructure and Mechanical Properties." *Journal of Alloys and Compounds* 707: 287–290. doi:10.1016/j.jallcom.2016.11.210.

Wang, Minbo, Ruidi Li, Tiechui Yuan, Chao Chen, Libo Zhou, Hui Chen, Mei Zhang, and Siyao Xie. 2019. "Microstructures and Mechanical Property of AlMgScZrMn - A Comparison Between Selective Laser Melting, Spark Plasma Sintering and Cast." *Materials Science and Engineering: A*, doi:10.1016/j.msea.2019.04.060.

Wang, D., L. Liu, G. Deng, C. Deng, Y. Bai, Y. Yang, W. Wu, et al. 2022. "Recent Progress on Additive Manufacturing of Multi-Material Structures with Laser Powder bed Fusion." *Virtual and Physical Prototyping* 17 (2): 329–365. doi:10.1080/17452759.2022.2028343.

Wang, Pei, Sijie Yu, Jaskarn Shergill, Anil Chaubey, Jürgen Eckert, Konda Gokuldoss Prashanth, and Sergio Scudino. 2021b. "Selective Laser Melting of Al-7Si-0.5Mg-0.5Cu: Effect of Heat Treatment on Microstructure Evolution, Mechanical Properties and Wear Resistance." *Acta Metallurgica Sinica (English Letters)*, doi:10.1007/s40195-021-01279-1.

Wang, Feng, Baohong Zhu, Baiqing Xiong, Yongan Zhang, Hongwei Liu, and Ronghua Zhang. 2007. "An Investigation on the Microstructure and Mechanical Properties of Spray-Deposited Al-8.5Fe-1.1V-1.9Si Alloy." *Journal of Materials Processing Technology* 183 (2-3): 386–389. doi:10.1016/j.jmatprotec.2006.10.033.

Waqar, Saad, Kai Guo, and Jie Sun. 2021. "FEM Analysis of Thermal and Residual Stress Profile in Selective Laser Melting of 316L Stainless Steel." *Journal of Manufacturing Processes* 66: 81–100. doi:10.1016/j.jmapro.2021.03.040.

Waqar, Saad, Kai Guo, and Jie Sun. 2022. "Evolution of Residual Stress Behavior in Selective Laser Melting (SLM) of 316L

Stainless Steel Through Preheating and in-Situ re-Scanning Techniques." *Optics & Laser Technology* 149, doi:10.1016/j.optlastec.2021.107806.

Waqar, Saad, Qidong Sun, Jiangwei Liu, Kai Guo, and Jie Sun. 2020. "Numerical Investigation of Thermal Behavior and Melt Pool Morphology in Multi-Track Multi-Layer Selective Laser Melting of the 316L Steel." *The International Journal of Advanced Manufacturing Technology* 112 (3-4): 879–895. doi:10.1007/s00170-020-06360-0.

Wu, Hong, Yaojia Ren, Junye Ren, Luxin Liang, Ruidi Li, Qihong Fang, Anhui Cai, Quan Shan, Yingtao Tian, and Ian Baker. 2021. "Selective Laser Melted AlSi10Mg Alloy Under Melting Mode Transition: Microstructure Evolution, Nanomechanical Behaviors and Tensile Properties." *Journal of Alloys and Compounds* 873, doi:10.1016/j.jallcom.2021.159823.

Xi, L., P. Wang, K. G. Prashanth, H. Li, H. V. Prykhodko, S. Scudino, and I. Kaban. 2019. "Effect of TiB2 Particles on Microstructure and Crystallographic Texture of Al-12Si Fabricated by Selective Laser Melting." *Journal of Alloys and Compounds* 786: 551–556. doi:10.1016/j.jallcom.2019.01.327.

Xian, J. W., S. A. Belyakov, M. Ollivier, K. Nogita, H. Yasuda, and C. M. Gourlay. 2017a. "Cu6Sn5 Crystal Growth Mechanisms During Solidification of Electronic Interconnections." *Acta Materialia* 126: 540–551. doi:10.1016/j.actamat.2016.12.043.

Xian, J. W., Z. L. Ma, S. A. Belyakov, M. Ollivier, and C. M. Gourlay. 2017b. "Nucleation of tin on the Cu6Sn5 Layer in Electronic Interconnections." *Acta Materialia* 123: 404–415. doi:10.1016/j.actamat.2016.10.008.

Yan, Qiqi, Dingfa Fu, Xuefeng Deng, Hui Zhang, and Zhenhua Chen. 2007. "Tensile Deformation Behavior of Spray-Deposited FVS0812 Heat-Resistant Aluminum Alloy Sheet at Elevated Temperatures." *Materials Characterization* 58 (6): 575–579. doi:10.1016/j.matchar.2006.06.024.

Yaneva, S., A. Kalkanlı, K. Petrov, R. Petrov, Ir Yvan Houbaert, and S. Kassabov. 2004. "Structure Development in Rapidly Solidified Al-Fe-V-Si Ribbons." *Materials Science and Engineering: A* 373 (1-2): 90–98. doi:10.1016/j.msea.2003.12.034.

Yang, Y., C. Ling, M. Yang, L. Yang, D. Wang, S. Peng, and C. Shuai. 2022. "Selective Laser Melted Rare Earth Magnesium Alloy with High Corrosion Resistance." *International Journal of Bioprint* 8 (3): 574. doi:10.18063/ijb.v8i3.574.

Yang, Y., Y. Zhu, M. M. Khonsari, and H. Yang. 2019. "Wear Anisotropy of Selective Laser Melted 316L Stainless Steel." *Wear* 428-429: 376–386. doi:10.1016/j.wear.2019.04.001.

Yu, Wenhui, Zhen Xiao, Xuhui Zhang, Yetao Sun, Peng Xue, Shuai Tan, Yongling Wu, and Hongyu Zheng. 2022. "Processing and Characterization of Crack-Free 7075 Aluminum Alloys with Elemental Zr Modification by Laser Powder bed Fusion." *Materials Science in Additive Manufacturing* 1 (1), doi:10.18063/msam.v1i1.4.

Zhang, L. C., D. Klemm, J. Eckert, Y. L. Hao, and T. B. Sercombe. 2011. "Manufacture by Selective Laser Melting and Mechanical Behavior of a Biomedical Ti-24Nb-4Zr-8Sn Alloy." *Scripta Materialia* 65 (1): 21–24. doi:10.1016/j.scriptamat.2011.03.024.

Zhao, D., C. Han, B. Peng, T. Cheng, J. Fan, L. Yang, L. Chen, and Q. Wei. 2022a. "Corrosion Fatigue Behavior and Anti-Fatigue Mechanisms of an Additively Manufactured Biodegradable Zinc-Magnesium Gyroid Scaffold." *Acta biomaterialia*, doi:10.1016/j.actbio.2022.09.047.

Zhao, Junhao, Binbin Wang, Tong Liu, Liangshun Luo, Yanan Wang, Xiaonan Zheng, Liang Wang, et al. 2022b. "A Study on Overlapping Effect of Melt Pools in Powder Bed Fusion Based on a Novel Prediction Method." *Additive Manufacturing* 59, doi:10.1016/j.addma.2022.103151.

Zheng, Lijing, Yingying Liu, Shaobo Sun, and Hu Zhang. 2015. "Selective Laser Melting of Al-8.5Fe-1.3V-1.7Si Alloy: Investigation on the Resultant Microstructure and Hardness." *Chinese Journal of Aeronautics* 28 (2): 564–569. doi:10.1016/j.cja.2015.01.013.

Zhou, Xin, Kailun Li, Dandan Zhang, Xihe Liu, Jing Ma, Wei Liu, and Zhijian Shen. 2015. "Textures Formed in a CoCrMo Alloy by Selective Laser Melting." *Journal of Alloys and Compounds* 631: 153–164. doi:10.1016/j.jallcom.2015.01.096.